

NAVAL POSTGRADUATE SCHOOL MONTEREY, CALIFORNIA



THESIS

**EXPERIMENTAL VERIFICATION OF AN OPTIMAL
LINEAR CONTROLLER FOR A FLEXIBLE
STRUCTURE**

by

William Burke Harrington, Jr.

December 1995

Thesis Advisor:

Brij N. Agrawal

Approved for public release; distribution is unlimited.

19960315 044

DTIC QUALITY INSPECTED 1

REPORT DOCUMENTATION PAGE			Form Approved OMB No. 0704-0188	
Public reporting burden for this collection of information is estimated to average 1 hour per response, including the time for reviewing instruction, searching existing data sources, gathering and maintaining the data needed, and completing and reviewing the collection of information. Send comments regarding this burden estimate or any other aspect of this collection of information, including suggestions for reducing this burden, to Washington Headquarters Services, Directorate for Information Operations and Reports, 1215 Jefferson Davis Highway, Suite 1204, Arlington, VA 22202-4302, and to the Office of Management and Budget, Paperwork Reduction Project (0704-0188) Washington DC 20503.				
1. AGENCY USE ONLY (Leave blank)		2. REPORT DATE December 1995		3. REPORT TYPE AND DATES COVERED Engineer's Thesis
4. TITLE AND SUBTITLE EXPERIMENTAL VERIFICATION OF AN OPTIMAL LINEAR CONTROLLER FOR A FLEXIBLE STRUCTURE			5. FUNDING NUMBERS	
6. AUTHOR(S) Harrington, William Burke Jr.				
7. PERFORMING ORGANIZATION NAME(S) AND ADDRESS(ES) Naval Postgraduate School Monterey CA 93943-5000			8. PERFORMING ORGANIZATION REPORT NUMBER	
9. SPONSORING/MONITORING AGENCY NAME(S) AND ADDRESS(ES)			10. SPONSORING/MONITORING AGENCY REPORT NUMBER	
11. SUPPLEMENTARY NOTES The views expressed in this thesis are those of the author and do not reflect the official policy or position of the Department of Defense or the U.S. Government.				
12a. DISTRIBUTION/AVAILABILITY STATEMENT Approved for public release; distribution is unlimited.			12b. DISTRIBUTION CODE	
13. ABSTRACT (<i>maximum 200 words</i>) Nanometer accuracy in many space applications requires that sensors be isolated from vibration disturbances by the main spacecraft body. The Flexible Spacecraft Simulator (FSS) at the Naval Postgraduate School is designed for testing multiple control system designs. The experimental setup simulates a microgravity environment for a flexible structure. A twenty-four state finite element model is used to characterize the flexible appendage. Piezoelectric ceramic wafers bonded to the structure are the actuators and sensors. A <i>VisionServer</i> external infrared camera provides direct feedback of the flexible structure's elbow and tip displacements to sub-millimeter accuracy. A Multiple-Input-Multiple-Output (MIMO) Linear Quadratic Gaussian (LQG) controller is experimentally compared with a Positive Position Feedback/Velocity feedback controller. The damping is increased on the order of 825% for both control implementations. The objective is to minimize the disturbance of the tip of the flexible structure, representing the reflector support point.				
14. SUBJECT TERMS Optimal control, Linear Quadratic Regulator, LQR, Linear Quadratic Gaussian, LQG, Smart Structures, Experimental verification			15. NUMBER OF PAGES 111	
			16. PRICE CODE	
17. SECURITY CLASSIFICATION OF REPORT Unclassified	18. SECURITY CLASSIFICATION OF THIS PAGE Unclassified	19. SECURITY CLASSIFICATION OF ABSTRACT Unclassified	20. LIMITATION OF ABSTRACT UL	

Approved for public release; distribution is unlimited.

**EXPERIMENTAL VERIFICATION OF AN OPTIMAL LINEAR CONTROLLER
FOR A FLEXIBLE STRUCTURE**

William Burke Harrington, Jr.
Lieutenant Commander, United States Navy
B. S. Marine Engineering, U. S. Naval Academy, 1985

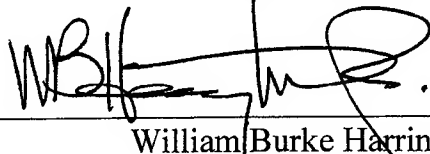
Submitted in partial fulfillment
of the requirements for the degree of

AERONAUTICAL AND ASTRONAUTICAL ENGINEER

from the

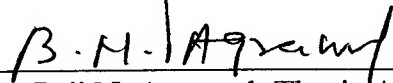
**NAVAL POSTGRADUATE SCHOOL
December 1995**

Author: _____

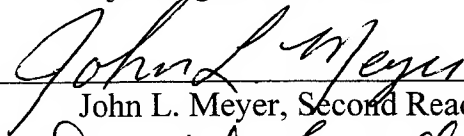


William Burke Harrington, Jr.

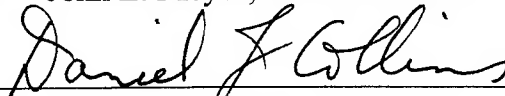
Approved by: _____



Brij N. Agrawal, Thesis Advisor



John L. Meyer, Second Reader



Daniel J. Collins, Chairman

Department of Aeronautical and Astronautical Engineering

ABSTRACT

Nanometer accuracy in many space applications requires that sensors be isolated from vibration disturbances by the main spacecraft body. The Flexible Spacecraft Simulator (FSS) at the Naval Postgraduate School is designed for testing multiple control system designs. The experimental setup simulates a microgravity environment for a flexible structure. A twenty-four state finite element model is used to characterize the flexible appendage. Piezoelectric ceramic wafers bonded to the structure are the actuators and sensors. A *VisionServer* external infrared camera provides direct feedback of the flexible structure's elbow and tip displacements to sub-millimeter accuracy. A Multiple-Input-Multiple-Output (MIMO) Linear Quadratic Gaussian (LQG) controller is experimentally compared with a Positive Position Feedback/Velocity feedback controller. The damping is increased on the order of 825% for both control implementations. The objective is to minimize the disturbance of the tip of the flexible structure, representing the reflector support point.

TABLE OF CONTENTS

I. INTRODUCTION	1
II. SCOPE OF THESIS	3
III. OPTIMAL CONTROL THEORY	5
A. BACKGROUND	5
B. STATE-SPACE REPRESENTATION	5
C. TRANSFORMATION OF STATE	6
D. OPTIMAL CONTROL THEORY	7
E. CONTROLLABILITY AND OBSERVABILITY	10
IV. PIEZOELECTRIC THEORY	13
A. HISTORY OF PIEZOELECTRICITY	13
B. FLEXIBLE SPACECRAFT SIMULATOR PIEZOCERAMIC ACTUATORS AND SENSORS	18
V. FINITE ELEMENT ANALYSIS	21
A. BACKGROUND	21
B. ELEMENT STIFFNESS MATRIX	21
C. ELEMENT MASS MATRIX	24
D. ASSEMBLING THE GLOBAL MASS AND STIFFNESS MATRICES INTO THE COMPLETE SYSTEM	26
E. PIEZOELECTRIC FINITE ELEMENT MODELING	27
VI. VISIONSERVER CAMERA SYSTEM	33
VII. ANALYTICAL MODEL	37

A.	FINITE ELEMENT MODEL	37
B.	SIMULATION RESULTS.....	40
VIII.	EXPERIMENTAL SETUP	45
A.	OVERVIEW.....	45
B.	AC-100 REAL-TIME CONTROLLER SETUP	49
C.	VISIONSERVER SETUP	52
IX.	EXPERIMENTAL PROCEDURE AND RESULTS.....	55
A.	BIAS REMOVAL AND COORDINATE TRANSFORMATION	55
B.	FILTERING	58
C.	INITIAL CONDITION RESPONSE	58
D.	ESTIMATOR VERIFICATION	60
E.	CONTROLLER TESTING AND EVALUATION.....	62
F.	DAMPING SUMMARY.....	71
X.	CONCLUSIONS AND RECOMMENDATIONS.....	73
A.	SUMMARY	73
B.	CONCLUSIONS	73
C.	RECOMMENDATIONS	74
	REFERENCES	75
	APPENDIX A. VISIONSERVER SETUP AND SOFTWARE	77
	APPENDIX B. SYSTEM MATRICES	85
	APPENDIX C. ANALYTICAL MODEL MODESHAPES	93
	INITIAL DISTRIBUTION LIST	97

ACKNOWLEDGEMENTS

I would like to acknowledge those people that made this second thesis possible. First of all, my wife, Angela, and my two boys, Burke and John. They put up with me after graduation so I could get this to press before we left. Thank you for your patience and putting up with my late nights and long days. This thesis would not have been possible without your full and loving support. Next, my thesis advisors, Professor Agrawal, Professor Cristi, and Professor Meyer, who all kept encouraging me when I felt burned out. Thank you for your dedication and extra effort to help me through. I will always be grateful for your support and encouragement. John, good luck and God bless with your new addition in January. And last but not least, Rafe Bailey our Lab manager and technician and Doug Seivwright our engineer were both extremely helpful and versatile in helping me construct the experiment and complete the work. Thanks to you both. Mele Kalikimaka, Rafe.

I. INTRODUCTION

The rapid advancement of space sensor technology and the requirement for nanometer accuracy has created a need for minimum vibration noise, high precision mounting platforms in space. The consumer's demand for high resolution imagery, large space structures, and precise position and attitude determination has produced a large body of advanced research in the field of structural control. Concurrent to the rapid increase in accuracy and resolution of sensor payloads is the need to isolate payloads from the disturbances inherent to any spacecraft.

For these types of applications, smart structures are a promising technology. In general, smart structures are the system elements that sense the dynamic state and change the system's structural properties, such as its natural frequencies and damping, to meet given performance objectives.

There are several types of embedded sensors and actuators which can be used for vibration and structural control. The embedded sensors are piezoelectric deformation sensors, strain gages, and fiber optic sensors. The embedded actuators are piezoceramic wafers, electrostrictive ceramic wafers, piezoceramic polymer film and shape memory metal wires. Piezoceramic sensors have a high strain sensitivity, a low noise baseline, low to moderate temperature sensitivity, and an ease of implementation. Piezoceramic actuators have high stiffness, sufficient stress to control vibration, good linearity, temperature insensitivity, are easy to implement, and minimize power consumption.

Conventional control methods have worked well in the past, but new design methods are required to obtain improved performance and robustness characteristics from

the structural control system in order to satisfy future design specifications. Positive position feedback (PPF) and velocity feedback are two proven methods of structural control that work well with piezoceramic actuators and sensors. With a multiple-input-multiple-output (MIMO) control system, linear quadratic control methods are a preferred choice.

Linear quadratic control is based on full state feedback. If all the states are not known, an observer is inserted into the loop to estimate the unknown states. Linear quadratic controllers using state estimate feedback are optimal for the nominal plant models but the performance may be far from satisfactory in real life due to plant uncertainties, unmodeled plant dynamics, and sensor noise that is unaccounted for in the system compensator. Attractive passband robustness properties of full state feedback optimal quadratic designs may disappear with the introduction of a state estimator. The Linear Quadratic Gaussian methodology provides an integrated frequency domain and state space approach for design of MIMO control systems.

This work concerns experimental verification of a LQG controller design [Ref. 1]. The design will be implemented on the NPS Flexible Spacecraft Simulator using two piezoceramic stack actuators and two piezoceramic sensors with an external optical infrared camera system to provide the feedback to the controller.

II. SCOPE OF THESIS

The objective of this research is to damp out the vibrations of a flexible antenna support structure. The flexible spacecraft simulator (FSS) in the Spacecraft Dynamics and Control laboratory will be used to experimentally verify the data obtained from an analytical LQG model [Ref.1]. In addition, an external infrared optical sensor will be employed to provide structure position and velocity information to the optimal controller.

The experimental procedure will be to first zero out the bias values of the sensors, execute the initial condition procedure, then test the various controller schemes. The use of multiple sensors and actuators will enable the controller to quickly dampen out higher order modes of the disturbance. The optimal controller will be compared against a known effective control scheme such as Positive Position Feedback (PPF) with derivative feedback control.

The format for the work is laid out as follows. The Chapters III through V will provide the background and theory used to develop the LQG controller, namely optimal control theory, finite element analysis, and piezoelectric theory. Chapter VI will give a description of the *VisionServer* camera system followed by Chapter VII which will summarize the analytical model design from Reference 1. Chapter VIII will explain the experimental setup used for this thesis, Chapter IX will describe the experimental procedure and results, and Chapter X will present conclusions and recommendations.

III. OPTIMAL CONTROL THEORY

A. BACKGROUND

State-space methods are the cornerstone of modern control theory. The essential difference between modern control theory and classical control theory is the characterization of a process by differential equations instead of transfer functions. In the modern approach, processes are represented by systems of coupled, first-order differential equations. In principle, there is no limit to the order of the system and in practice the limit is the computational cost to perform the required calculations reliably.

B. STATE-SPACE REPRESENTATION

Second-order differential equations can be expressed as a set of simultaneous first-order equations. They are represented in state-variable form as the vector equations

$$\begin{aligned}\dot{\mathbf{x}} &= \mathbf{f}(\mathbf{x}, \mathbf{u}) \\ \mathbf{y} &= \mathbf{h}(\mathbf{x}, \mathbf{u})\end{aligned}\tag{3.1}$$

where the input is \mathbf{u} , and the output is \mathbf{y} .

The column vector \mathbf{x} is called the state of the system and contains n elements for a n th-order system. For mechanical systems, the states usually consist of the positions and velocities of the separate bodies. The vector function \mathbf{f} relates the first derivative of the state to the state itself and the input \mathbf{u} . Parameters in the function \mathbf{f} could be dependent on time as well as position and velocity, but by and large, for structural systems the parameters can be considered time-invariant. Linear approximations will be used for

nonlinear systems in design and analysis. For the linear case, equation (3.1) can be written as

$$\begin{aligned}\dot{\mathbf{x}} &= \mathbf{Ax} + \mathbf{Bu} \\ \mathbf{y} &= \mathbf{Cx} + \mathbf{Du}\end{aligned}\tag{3.2a,b}$$

where \mathbf{A} is an $n \times n$ system matrix, \mathbf{B} is an $n \times m$ control matrix, \mathbf{C} is an $l \times n$ observer matrix and \mathbf{D} is an $l \times m$ feed-through matrix (direct transmission matrix). Under most circumstances \mathbf{D} is normally a null matrix.

C. TRANSFORMATION OF STATE

The description of the system given by equation (3.2) is not unique. Matrix algebra enables a linear transformation of state without changing the basic properties of a matrix. Consider a state vector \mathbf{z} where

$$\mathbf{x} = \mathbf{Tz}\tag{3.3}$$

and \mathbf{T} is a nonsingular matrix. Substituting equation (3.3) into equation (3.2a), a linear transformation of state is performed

$$\begin{aligned}\dot{\mathbf{x}} &= \mathbf{T}\dot{\mathbf{z}} = \mathbf{ATz} + \mathbf{Bu} \\ \dot{\mathbf{z}} &= \mathbf{T}^{-1}\mathbf{ATz} + \mathbf{T}^{-1}\mathbf{Bu} \\ \dot{\mathbf{z}} &= \mathbf{A_Tz} + \mathbf{B_Tu}\end{aligned}\tag{3.4}$$

where

$$\begin{aligned}\mathbf{A_T} &= \mathbf{T}^{-1}\mathbf{AT} \\ \mathbf{B_T} &= \mathbf{T}^{-1}\mathbf{B}\end{aligned}$$

Substituting equation (3.3) into equation (3.2b)

$$\begin{aligned}y &= \mathbf{CTz} + \mathbf{Du} \\ &= \mathbf{C_T z} + \mathbf{Du}\end{aligned}\tag{3.5}$$

where

$$\mathbf{C_T} = \mathbf{CT}$$

It is sometimes convenient to transform a physical system model into its *modal* canonical form, also known as the *Jordan* canonical form. This state description decouples the coupled first order equations into n independent first-order equations, providing that the system matrix is diagonalizable. This description has many advantages. It allows the characterization of the degree of control authority the input has on each mode, the observability of each mode, and the damping ratio of each damped mode.

D. OPTIMAL CONTROL THEORY

An effective and widely used control technique of linear control systems is the optimal Linear Quadratic Regulator (LQR). Provided the full state vector is observable, this method can be employed to fit specific design and performance criteria. A quadratic cost function is used to minimize the performance index, J . The general form for the LQR is

$$J = \int (\mathbf{x}^T \mathbf{Q} \mathbf{x} + \mathbf{u}^T \mathbf{R} \mathbf{u}) dt\tag{3.6}$$

where \mathbf{Q} is the state weighting matrix and \mathbf{R} is the control weighting matrix. The necessary conditions for the optimal solution are that \mathbf{Q} must be symmetric and positive semi-definite and \mathbf{R} must be symmetric and positive definite. The solution to the LQR problem results in the optimum full state feedback gain matrix

$$\mathbf{K} = \mathbf{R}^{-1}\mathbf{B}'\mathbf{M} \quad (3.7)$$

where \mathbf{M} satisfies the matrix Riccati equation

$$-\dot{\mathbf{M}} = \mathbf{M}\mathbf{A} + \mathbf{A}'\mathbf{M} - \mathbf{M}\mathbf{B}\mathbf{R}^{-1}\mathbf{B}'\mathbf{M} + \mathbf{Q} \quad (3.8a)$$

For a time-infinite solution, $\dot{\mathbf{M}}$ is set to zero. The control input is then

$$\mathbf{u} = -\mathbf{K}\mathbf{x} \quad (3.8b)$$

If the full state vector is not available it is necessary to design a state estimator or observer. The general form of an observer is given by

$$\dot{\hat{\mathbf{x}}} = \mathbf{A}\hat{\mathbf{x}} + \mathbf{B}\mathbf{u} + \mathbf{L}(y - \mathbf{C}\hat{\mathbf{x}}) \quad (3.9)$$

where $\hat{\mathbf{x}}$ is the estimated state vector and \mathbf{L} is the observer gain matrix. The inputs to the observer are the outputs from the plant and the control inputs to the plant.

By solving for the optimum observer gain, $\hat{\mathbf{L}}$, the observer is known as a Kalman filter. The general form of the dynamical equations used in Kalman filter synthesis are

$$\begin{aligned}\dot{\mathbf{x}} &= \mathbf{Ax} + \mathbf{Bu} + \mathbf{Fv} \\ y &= \mathbf{Cx} + \mathbf{Du} + w\end{aligned}\tag{3.10}$$

where \mathbf{F} is the plant uncertainty matrix, w is the state noise vector, and v is the sensor noise vector. Both v and w are considered to be white noise processes. White noise processes have the property of having a zero mean. This assumption does not always hold true in the real world but it simplifies the analysis considerably. The solution for the optimal observer gain is given by probability theory. The Kalman observer gain, $\hat{\mathbf{L}}$, is given by

$$\hat{\mathbf{L}} = \hat{\mathbf{P}}\mathbf{C}'\mathbf{W}^{-1}\tag{3.11}$$

where $\hat{\mathbf{P}}$ is taken from

$$\dot{\hat{\mathbf{P}}} = \mathbf{A}\hat{\mathbf{P}} + \hat{\mathbf{P}}\mathbf{A}' - \hat{\mathbf{P}}\mathbf{C}'\mathbf{W}^{-1}\mathbf{C}\hat{\mathbf{P}} + \mathbf{F}\mathbf{V}\mathbf{F}'\tag{3.12}$$

The process noise covariance matrices \mathbf{V} and \mathbf{W} are given by

$$\begin{aligned}E\{v(t)v'(t)\} &= \mathbf{V}(t)\delta(t-\tau) \\ E\{v(t)w'(t)\} &= \mathbf{X}(t)\delta(t-\tau) \\ E\{w(t)w'(t)\} &= \mathbf{W}(t)\delta(t-\tau)\end{aligned}\tag{3.13}$$

$\mathbf{X}(t)$ is the system cross-covariance matrix and is a function of the correlation of sensor noise to plant noise and under most circumstances is considered zero. The symbol $E\{ \}$ denotes mathematical expectation, which is the average computed in the probabilistic sense.

E. CONTROLLABILITY AND OBSERVABILITY

Controllability indicates the extent that the states are controllable via the control matrix, \mathbf{B} . Observability indicates the number of states that are observable via the sensors. They are two mutually independent functions of the system plant matrix, control matrix and the observer matrix. One simple test for controllability and observability is to form the controllability matrix (\mathbf{M}_c) and the observability matrix (\mathbf{M}_o). If each matrix is of full rank the states are independent of one another and can be controlled or observed. The degree of controllability or observability cannot be determined from this test. Converting the system to *Jordan* canonical form, however, will help indicate the relative control authority to the individual modal states and also the relative observability for each modal state. An element with a value of zero indicates that it is detached from the controller or sensor and the larger the element's absolute value the more controllable or observable a state is in relation to other modes.

The following are the equations for the respective matrices:

$$\begin{aligned}\mathbf{M}_c &= [\mathbf{B} \quad \mathbf{AB} \quad \mathbf{A}^2\mathbf{B} \quad \dots \quad \mathbf{A}^{n-1}\mathbf{B}] \\ \mathbf{M}_o &= [\mathbf{C}^T \quad \mathbf{A}^T\mathbf{C}^T \quad (\mathbf{A}^T)^2\mathbf{C}^T \quad \dots \quad (\mathbf{A}^T)^{n-1}\mathbf{C}^T]^T\end{aligned}\tag{3.14}$$

A complete treatment is given in several textbooks, such as [Refs. 2,3]. These concepts will play a fundamental role in the design of the control system for the flexible structure. The whole concept of control design is a compromise between accuracy, complexity, and robustness. In particular, as this thesis will show, a very accurate model of the system might not only be too complex, but also might be bound to be uncontrollable or unobservable. This is because an exact model is likely to contain a number of states, i.e. modes, which are hard to completely control with the given input signals. Likewise these same states might not be easily observable. When this is the case, the designer would look for a simpler model where all the states are controllable and observable, and the effect of the neglected states will be within the noise level. For this problem the controllability and observability matrices give a clear indication on the characteristics of the model.

IV. PIEZOELECTRIC THEORY

A. HISTORY OF PIEZOELECTRICITY

Piezoelectricity is a phenomenon that describes certain materials that generate electricity when a mechanical stress is applied. This is known as the direct effect. Conversely, when an electric field is applied to them a mechanical stress is generated. Piezoelectricity occurs naturally in some crystalline materials and can be induced in other polycrystalline materials through a process known as “poling”. The material’s crystal lattice structure may be poled by the application of a large electric field, usually at high temperature (see Figure 4.1). [Ref. 4]

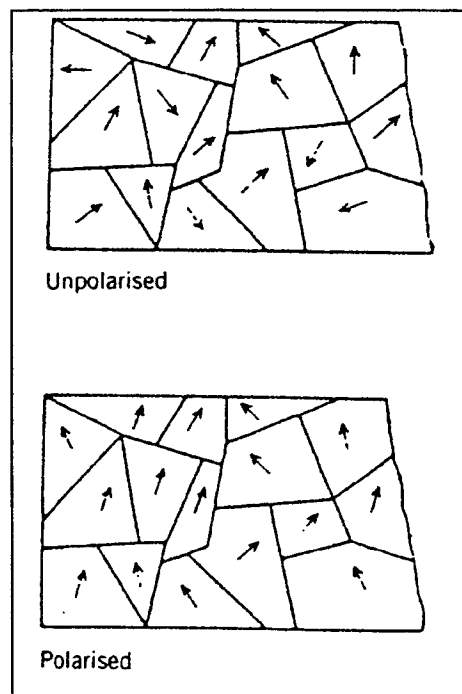


Figure 4.1. [Ref. 4] Crystalline Lattice Structures

Subsequent application of an electric field will produce additive strains locally which translate into a global strain for the material. The direct piezoelectric effect has been used for a long time in sensors such as accelerometers. Use of the converse effect has been restricted to ultrasonic transducers until recently. Barium titanate, discovered in the 1940s, was the first widely used piezoceramic. Lead zirconate titanate (PZT), discovered in 1954 [Ref. 5], has now largely superseded barium titanate because of its stronger piezoelectric effects. Only recently have researchers in the area of structural control taken notice of the very desirable features of piezoelectric actuators and have started using them for many structural control applications. Piezoceramics are compact, have a very good frequency response, and can be easily incorporated into structural systems. Actuation strains on the order of 1000 μ strain have been reported for PZT material. Strains are non-dimensional ratios of the change in length to the original length for a given impetus. Within the linear range piezoceramics produce strains that are proportional to the applied electric field/voltage. These features make them very attractive for structural control applications.

There are several methods to model the constitutive behavior of piezoelectric materials. The most popular is the macromechanical approach, it provides the relationship between the electrical and mechanical effects in a manner that can be incorporated into typical isotropic or orthotropic structural materials. For linear piezoelectric materials, the interaction between the electrical and mechanical variables can be described by linear relations of the form

$$\begin{aligned} S_i &= s_{ij}^E T_j + d_{mi} E_m \\ D_m &= d_{mi} T_i + \epsilon_{mk}^T E_k \end{aligned} \quad (4.1)$$

The mechanical variables are the stress T and the strain S , and the electrical variables are the electric field E and the electric displacement D ; s is the compliance, d is the piezoelectric constant and ϵ is the permittivity. The first equation describes the converse piezoelectric effect, and the second equation describes the direct effect. The stress and strain are second order tensors, while the electric field and electric displacement are first order.

Figure 4.2 shows the typical coordinate system used to represent a poled piezoelectric. The 3-axis is in the direction of the initial polarization.

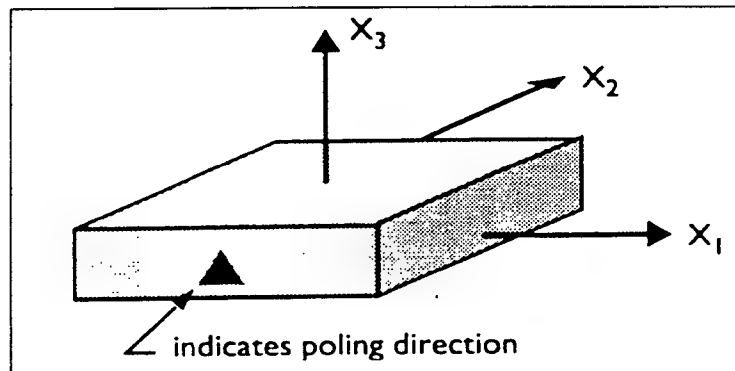


Figure 4.2. [Ref. 4] Typical Piezoceramic Coordinate System

The 1 and 2-axes are arbitrary in the plane perpendicular to the poling direction. The 1 and 2-axes are arbitrary because a poled piezoelectric is transversely isotropic in the 1–2 plane. The equations above written explicitly in matrix form are

$$\begin{bmatrix} S_1 \\ S_2 \\ S_3 \\ S_4 \\ S_5 \\ S_6 \\ D_1 \\ D_2 \\ D_3 \end{bmatrix} = \begin{bmatrix} s_{11}^E & s_{12}^E & s_{13}^E & 0 & 0 & 0 & 0 & 0 & d_{31} \\ s_{12}^E & s_{11}^E & s_{13}^E & 0 & 0 & 0 & 0 & 0 & d_{31} \\ s_{13}^E & s_{13}^E & s_{33}^E & 0 & 0 & 0 & 0 & 0 & d_{33} \\ 0 & 0 & 0 & s_{55}^E & 0 & 0 & 0 & d_{15} & 0 \\ 0 & 0 & 0 & 0 & s_{55}^E & 0 & d_{15} & 0 & 0 \\ 0 & 0 & 0 & 0 & 0 & s_{66}^E & 0 & 0 & 0 \\ 0 & 0 & 0 & 0 & d_{15} & 0 & \epsilon_1^T & 0 & 0 \\ 0 & 0 & 0 & d_{15} & 0 & 0 & 0 & \epsilon_1^T & 0 \\ d_{31} & d_{31} & d_{33} & 0 & 0 & 0 & 0 & 0 & \epsilon_3^T \end{bmatrix} \begin{bmatrix} T_1 \\ T_2 \\ T_3 \\ T_4 \\ T_5 \\ T_6 \\ E_1 \\ E_2 \\ E_3 \end{bmatrix} \quad (4.2)$$

Where S_1 through S_3 are the normal strains, S_4 through S_6 are the shear strains, T_1 through T_3 are the normal stresses, T_4 through T_6 are the shear stresses, D_1 through D_3 are the electric displacements and E_1 through E_3 are the electric fields associated with the given coordinate system.

The piezoelectric constants that are of most interest from a structural standpoint are the d constants. These constants relate the strain developed in the material to the applied electric field; obviously, the highest value of these constants is desirable. The d_{33} constant relates the strain in the 3-direction to the field in the 3-direction.; similarly, the d_{31} relates the strain in the 1-direction to the electric field in the 3-direction. The electric field is voltage applied across the piezoelectric divided by its thickness. It is important to point out that usually d_{33} is positive and d_{31} is negative. This means that a positive field (i.e., a field applied in the poling direction) will produce a positive mechanical strain in the 3-direction and a negative strain in the 1-direction.

There are many applications for the use of PZT actuators and they can be divided into two general categories: linear actuators and actuators used for structural control

applications. In the first category, PZT actuators arranged in the form of stacks are used in a fashion similar to shakers or conventional hydraulic or electrical actuators. Due to the fact that the stroke is severely limited, in static applications they are used only for micropositioning work. In structural control applications, the actuators are typically embedded or bonded to the surfaces of the structure and apply localized strains that can be used directly to control structural deformations. A typical arrangement is shown in Figure 4.3; the two actuators are on the upper and lower surfaces of the structure and are actuated out of phase (the upper expands and the lower contracts), which creates a moment on the structure. [Ref. 4]

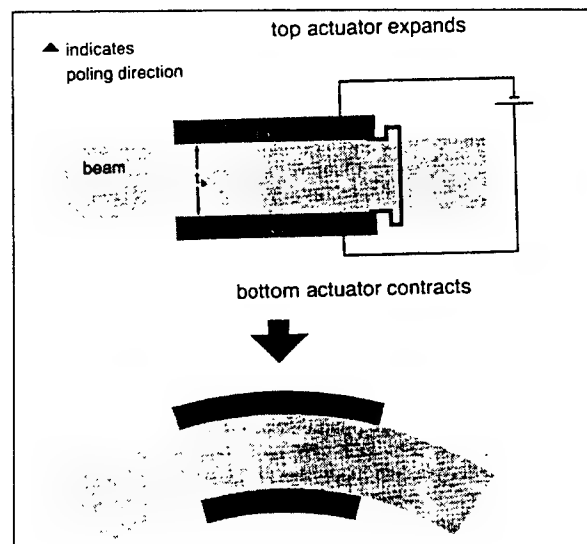


Figure 4.3. [Ref. 4] Piezoceramic Actuator Pair

In the remainder of this chapter we will apply piezoceramic actuators and sensors as structural control elements.

B. FLEXIBLE SPACECRAFT SIMULATOR PIEZOCERAMIC ACTUATORS AND SENSORS

Piezoceramic sensors and actuators are located on the flexible appendage as shown in Figure 4.4. The piezoceramic wafers are bonded to the surface of the flexible arm and the voltage developed from the sensors is fed to the actuators by way of the designed control system.

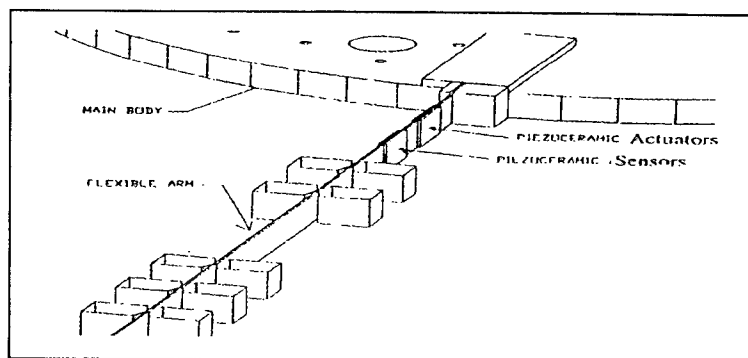


Figure 4.4. Piezoceramic Actuators and Sensors Mounted on the FSS Flexible Beam

Figure 4.5 illustrates the orientation of a piezoceramic wafer on an arm and the alignment of its axis that describes the electro-mechanical relationships.

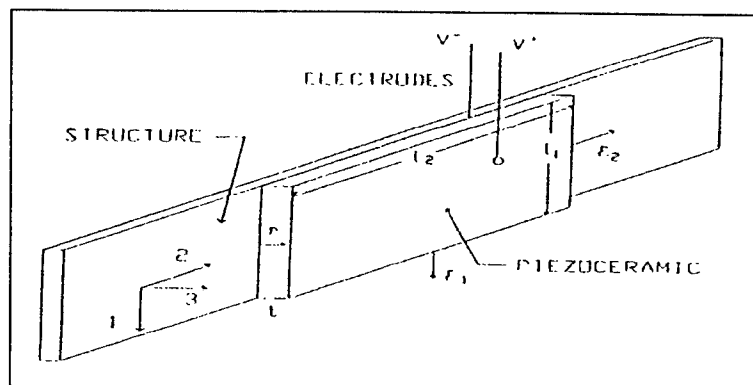


Figure 4.5. Poled Piezoceramic Mounted on FSS Beam

The piezoceramic wafers in a sensory mode produce a charge between their electrodes that is directly proportional to the lateral strains. It is given by

$$Q = AEd_{31}(\epsilon_1 + \epsilon_2) \quad (4.3)$$

where A is the lateral area of the piezoceramic wafer, E is Young's modulus of the wafer, d_{31} is the lateral charge coefficient, and ϵ_1 and ϵ_2 are the strain values in the lateral directions respectively. The capacitance for a piezoceramic wafer as shown in Figure 4.5 is given by

$$C = \frac{DA}{t} \quad (4.4)$$

where D is the dielectric constant of the piezoceramic and t is the thickness of the wafer.

The voltage V produced by a sensor under strain is given by

$$V = \frac{Q}{C} = \frac{Ed_{31}}{D}t(\epsilon_1 + \epsilon_2) \quad (4.5)$$

When using piezoceramic wafers as actuators, the attachment geometry is similar to the sensor geometry shown in Figure 4.5. The control voltage, e_c , is applied to the wafers and the lateral strain that is developed can act to control the bending of the beam. The electric field that is developed by the wafer is given by

$$\Phi = \frac{VC}{t_p} \quad (4.6)$$

Care must be taken not to induce a strong electric field that is opposed to the piezoceramic's poling direction as that can damage the material by depolarizing it. Typical field limits by most materials are between 500 and 1000 volts/mm.

V. FINITE ELEMENT ANALYSIS

A. BACKGROUND

The need for characterization of complex structures and the advent of the modern day computer has given rise to a method of analysis known as the finite element method. The idea behind the finite element method is to provide a formulation which can exploit digital computer automation for the analysis of irregular systems. To this end, the method regards a complex structure as an assemblage of finite elements, each of which is part of a continuous structural member. By requiring that displacements be compatible and internal forces be balanced at points shared by elements, known as nodes, the entire structure is compelled to act as one entity.

The finite element method of analysis, while considering a continuous structure, is a discretization problem. It expresses the displacements of the continuous structure in terms of a finite number of displacements at the nodal points multiplied by interpolation functions. The advantage of the finite element method over any other method is that system equations can be derived by first deriving the equations for a single element and then assembling them by using constraint conditions. The displacement at any point inside the element is obtained by means of interpolation, where the interpolation functions are generally low-degree polynomials and are identical for every element. [Ref. 6]

B. ELEMENT STIFFNESS MATRIX

Meirovitch [Ref. 6, pp. 303-304] uses the direct method for derivation of the elemental stiffness matrix. The stiffness matrix relates a displacement vector to a force

vector. Using the element in Figure 5.1, for uniform bending stiffness, the differential equation for the displacement $w(x)$ is

$$EI \frac{d^4 w(x)}{dx^4} = 0 \quad 0 < x < h \quad (5.1)$$

where E is Young's modulus for the material and I is the area moment of inertia for the beam cross-section.

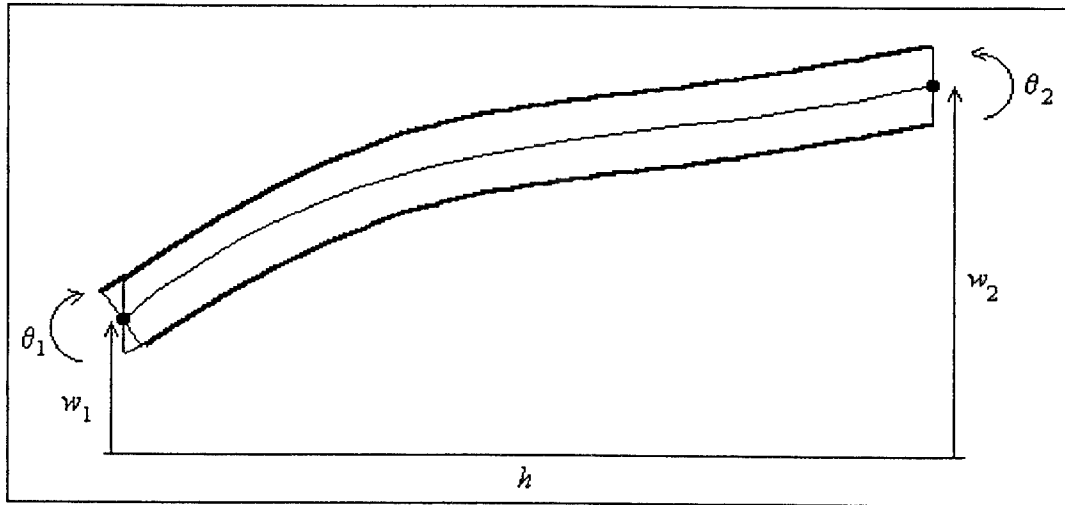


Figure 5.1. Beam Element for Finite Element Model

By integrating four times, we have the elemental displacement at any point

$$w(x) = \frac{1}{6}c_1x^3 + \frac{1}{2}c_2x^2 + c_3x + c_4 \quad (5.2)$$

with c_1 through c_4 as the constants of integration, determined from the boundary conditions

$$w(0) = w_1 \quad \left. \frac{dw(x)}{dx} \right|_{x=0} = \theta_1 \quad w(h) = w_2 \quad \left. \frac{dw(x)}{dx} \right|_{x=h} = \theta_2 \quad (5.3)$$

w_1 and w_2 are the nodal displacements and θ_1 and θ_2 are the nodal rotations at the endpoints of the element. By solving equation (5.2) into (5.3) the corresponding constants of integration are solved as

$$\begin{aligned} c_1 &= \frac{6}{h^3}(2w_1 + h\theta_1 - 2w_2 + h\theta_2) & c_2 &= \frac{2}{h^2}(-3w_1 - 2h\theta_1 + 3w_2 - h\theta_2) \\ c_3 &= \theta_1 & c_4 &= w_1 \end{aligned} \quad (5.4)$$

Hence, introducing equation (5.4) into (5.2), the expression for the bending displacement is determined to be

$$\begin{aligned} w(x) = & \left[1 - 3\left(\frac{x}{h}\right)^2 + 2\left(\frac{x}{h}\right)^3 \right] w_1 + \left[\frac{x}{h} - 2\left(\frac{x}{h}\right)^2 + \left(\frac{x}{h}\right)^3 \right] h\theta_1 \\ & + \left[3\left(\frac{x}{h}\right)^2 - 2\left(\frac{x}{h}\right)^3 \right] w_2 + \left[-\left(\frac{x}{h}\right)^2 + \left(\frac{x}{h}\right)^3 \right] h\theta_2 \end{aligned} \quad (5.5)$$

The bending displacement is related to the inter-element nodal forces f_1, f_2, f_3 , and f_4 as follows

$$\begin{aligned} EI \left. \frac{d^3 w(x)}{dx^3} \right|_{x=0} &= f_1 & EI \left. \frac{d^2 w(x)}{dx^2} \right|_{x=0} &= -f_2 \\ EI \left. \frac{d^3 w(x)}{dx^3} \right|_{x=h} &= -f_3 & EI \left. \frac{d^3 w(x)}{dx^3} \right|_{x=h} &= f_4 \end{aligned} \quad (5.6)$$

Combining equations (5.6) and (5.5) yields

$$\begin{aligned}
f_1 &= \frac{EI}{h^3} (12w_1 + 6h\theta_1 - 12w_2 + 6h\theta_2) \\
f_2 &= \frac{EI}{h^2} (6w_1 + 4h\theta_1 - 6w_2 + 2h\theta_2) \\
f_3 &= \frac{EI}{h^3} (-12w_1 - 6h\theta_1 + 12w_2 - 6h\theta_2) \\
f_4 &= \frac{EI}{h^2} (6w_1 + 2h\theta_1 - 6w_2 + 4h\theta_2)
\end{aligned} \tag{5.7}$$

This can be written in matrix form as

$$[k]\{q\} = \{f\} \tag{5.8}$$

where the nodal displacement vector and the nodal force vector are given by

$$\{q\} = \begin{Bmatrix} w_1 \\ \theta_1 \\ w_2 \\ \theta_2 \end{Bmatrix} \quad , \quad \{f\} = \begin{Bmatrix} f_1 \\ f_2 \\ f_3 \\ f_4 \end{Bmatrix} \tag{5.9}$$

and the element stiffness matrix is given by

$$[k] = \frac{EI}{h^3} \begin{bmatrix} 12 & 6h & -12 & 6h \\ 6h & 4h^2 & -6h & 2h^2 \\ -12 & -6h & 12 & -6h \\ 6h & 2h^2 & -6h & 4h^2 \end{bmatrix} \tag{5.10}$$

C. ELEMENT MASS MATRIX

Equation (5.5) can be written as a function of the nodal displacements and interpolation functions, $L(x)$

$$w(x) = L_1(x)w_1 + L_2(x)h\theta_1 + L_3(x)w_2 + L_4(x)h\theta_2 \quad (5.11)$$

where

$$\begin{aligned} L_1(x) &= \left[1 - 3\left(\frac{x}{h}\right)^2 + 2\left(\frac{x}{h}\right)^3 \right] & L_3(x) &= \left[3\left(\frac{x}{h}\right)^2 - 2\left(\frac{x}{h}\right)^3 \right] \\ L_2(x) &= \left[\frac{x}{h} - 2\left(\frac{x}{h}\right)^2 + \left(\frac{x}{h}\right)^3 \right] & L_4(x) &= \left[-\left(\frac{x}{h}\right)^2 + \left(\frac{x}{h}\right)^3 \right] \end{aligned} \quad (5.12)$$

Equations (5.11) and (5.12) can be expressed in matrix form

$$w(x, t) = \{L(x)\}^T \{x(t)\} \quad (5.13)$$

with $\{L(x)\}$ as a four-dimensional vector of the interpolation functions and $\{x(t)\}$ a four-dimensional vector of nodal displacements. The element kinetic energy has the form

$$T(t) = \frac{1}{2} \int_0^h m(x) \left[\frac{\partial^2 w(x, t)}{\partial t^2} \right]^2 dx = \frac{1}{2} \{\dot{w}(t)\}^T [m] \{\dot{w}(t)\} \quad (5.14)$$

where the 4×4 mass matrix is given by

$$[m] = \int_0^h m(x) \{L(x)\} \{L(x)\}^T dx \quad (5.15)$$

Inserting the interpolation functions vector, equation (5.12), into equation (5.15)

and integrating over the element length, the elemental mass matrix becomes

$$[m] = \frac{mh}{420} \begin{bmatrix} 156 & 22h & 54 & -13h \\ 22h & 4h^2 & 13h & -3h^2 \\ 54 & 13h & 156 & -22h \\ -13h & -3h^2 & -22h & 4h^2 \end{bmatrix} \quad (5.16)$$

D. ASSEMBLING THE GLOBAL MASS AND STIFFNESS MATRICES INTO THE COMPLETE SYSTEM

The next step is to assemble each element's mass and stiffness matrices into the global system mass matrix and the global system stiffness matrix, respectively. The assembling procedure is an algebraic process of summing the overlapping element matrices. Consider the 4×4 element matrix partitioned into a 2×2 matrix of 2×2 sub-matrices

$$[m^1] = \begin{bmatrix} m_{11}^1 & m_{12}^1 \\ m_{21}^1 & m_{22}^1 \end{bmatrix} \quad [m^2] = \begin{bmatrix} m_{11}^2 & m_{12}^2 \\ m_{21}^2 & m_{22}^2 \end{bmatrix} \quad \cdots \quad [m^n] = \begin{bmatrix} m_{11}^n & m_{12}^n \\ m_{21}^n & m_{22}^n \end{bmatrix} \quad (5.17)$$

The global system matrix is required to be symmetric and is constructed by adding the element matrices along the diagonal

$$[M] = \sum_1^n [m^n] \quad (5.18)$$

For example, with three elements this matrix becomes

$$[M] = \begin{bmatrix} m_{11}^1 & m_{12}^1 & 0 & 0 \\ m_{21}^1 & m_{22}^1 + m_{11}^2 & m_{12}^2 & 0 \\ 0 & m_{21}^2 & m_{22}^2 + m_{11}^3 & m_{12}^3 \\ 0 & 0 & m_{21}^3 & \ddots \end{bmatrix} \quad (5.19)$$

The method is the same for both the stiffness and the mass matrices. In order to satisfy the boundary conditions for a fixed-free system, the displacement and rotation at the root of the flexible appendage must be zero. This condition is satisfied by eliminating the first and second rows and the first and second columns from both the global mass and stiffness matrices, respectively.

E. PIEZOELECTRIC FINITE ELEMENT MODELING

The piezoceramic elements used in the structure must be incorporated into the finite element model. The basic equations for both piezoceramic actuators and sensors are the same as for ordinary structural elements discussed in the previous section. There is a need to compensate for the piezoceramic displacement from the center of the beam and Figure 5.2 illustrates this concept. In addition, the electro-mechanical relationships must be taken into account for implementation into an analytical model suitable for control design.

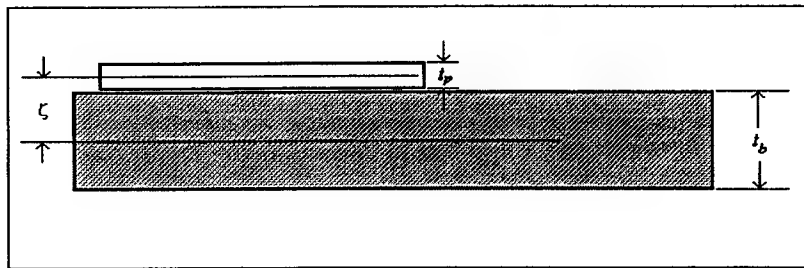


Figure 5.2. Piezoceramic Element Placement on Beam

From equation (4.1) the general relationship for the electro-mechanical coupling is given by

$$\begin{Bmatrix} D_3 \\ S_1 \end{Bmatrix} = \begin{bmatrix} \varepsilon_3^T & d_{31} \\ d_{31} & s_{11}^E \end{bmatrix} \begin{Bmatrix} E_3 \\ T_1 \end{Bmatrix} \quad (5.20)$$

Using the fact that the elastic constant for piezoceramic material, s , is the inverse of its Young's modulus, E_p , this equation can be written as

$$\begin{Bmatrix} D_3 \\ T_1 \end{Bmatrix} = \begin{bmatrix} \varepsilon_3^T - d_{31}^2 E_p & d_{31} E_p \\ -d_{31} E_p & E_p \end{bmatrix} \begin{Bmatrix} E_3 \\ S_1 \end{Bmatrix} \quad (5.21)$$

The next step is to set up the equation for the elemental potential energy, U .

$$-U = \frac{1}{2} \int_V (-T_1 S_1 + D_3 E_3) dV \quad (5.22)$$

where the two terms in the integral represent mechanical energy ($T_1 S_1$) and electrical energy ($D_3 E_3$). Using w_p as the width of the piezoceramic wafer, this equation can be rewritten as

$$\begin{aligned} -U &= \frac{1}{2} w_p \int_0^h \int_{\zeta}^{\zeta+t_p} (-T_1 S_1 + D_3 E_3) dx dz \\ &= \frac{1}{2} w_p \int_0^h \int_{\zeta}^{\zeta+t_p} \begin{Bmatrix} D_3 \\ T_1 \end{Bmatrix}^T \begin{bmatrix} 1 & 0 \\ 0 & -1 \end{bmatrix} \begin{Bmatrix} E_3 \\ S_1 \end{Bmatrix} dx dz \end{aligned} \quad (5.23)$$

The strain, S_1 , can be written using small angle displacement theory as

$$S_1 = \varepsilon_x = -z \frac{\partial^2 w}{\partial x^2} \quad (5.24)$$

substituting equation (5.21) into equation (5.23)

$$\begin{aligned}
 -U &= \frac{1}{2} w_p \int_0^h \int_{\zeta}^{\zeta+t_p} \begin{Bmatrix} E_3 \\ \epsilon_x \end{Bmatrix}^T \begin{bmatrix} \epsilon_3^T - d_{31}^2 E_p & d_{31} E_p \\ d_{31} E_p & -E_p \end{bmatrix} \begin{Bmatrix} E_3 \\ \epsilon_x \end{Bmatrix} dx dz \\
 &= \frac{1}{2} w_p \int_0^h \int_{\zeta}^{\zeta+t_p} \left[(\epsilon_3^T - d_{31}^2 E_p) E_3^2 + 2d_{31} E_p E_3 \epsilon_x - E_p \epsilon_x^2 \right] dx dz
 \end{aligned} \tag{5.25}$$

then, using equation (5.24)

$$-U = \frac{1}{2} w_p \int_0^h \int_{\zeta}^{\zeta+t_p} \left[(\epsilon_3^T - d_{31}^2 E_p) E_3^2 + 2d_{31} E_p E_3 z \frac{\partial^2 w}{\partial x^2} - E_p z^2 \left(\frac{\partial^2 w}{\partial x^2} \right)^2 \right] dx dz \tag{5.26}$$

Rewriting equation (5.13) in terms of a summation

$$w(x, t) = \sum_{i=1}^4 \Phi_i(x) q_i(t) \tag{5.27}$$

where Φ is the vector of interpolation functions or “modeshapes” and q is the nodal vector from equation (5.9a). Inserting this equation along with the interpolation functions, equation (5.12), the general form of the energy equation is

$$-U = \frac{1}{2} \gamma e^2 - q^T b e - \frac{1}{2} q^T k_p q \tag{5.28}$$

where

$$\begin{aligned}\gamma &= \frac{w_p h}{t_p} (\varepsilon_3^T - d_{31}^2 E_p), \quad e = t_p E_3 \\ b_i &= d_{31} E_p w_p \left(\zeta + \frac{t_p}{2} \right) \int_0^h \frac{d^2 \Phi_i(x)}{dx^2} dx \\ [k_p]_{ij} &= w_p E_p t_p \left[\zeta^2 + \zeta t_p + \frac{t_p^2}{3} \right] \int \frac{d^2 \Phi_i(x)}{dx^2} \frac{d^2 \Phi_j(x)}{dx^2} dx\end{aligned}$$

Substituting the interpolation functions from equation (5.12) into the b vector, we get

$$\begin{aligned}b_1 &= 0 \\ b_2 &= -d_{31} E_p w_p \left(\zeta + \frac{t_p}{2} \right) \\ b_3 &= 0 \\ b_4 &= d_{31} E_p w_p \left(\zeta + \frac{t_p}{2} \right)\end{aligned} \tag{5.29}$$

and into the piezoceramic elemental stiffness matrix, $[k_p]$

$$[k_p] = \frac{\kappa}{h} \begin{bmatrix} \frac{12}{h^2} & \frac{6}{h} & -\frac{12}{h^2} & \frac{6}{h} \\ \frac{6}{h} & 4 & -\frac{6}{h} & 2 \\ -\frac{12}{h^2} & -\frac{6}{h} & \frac{12}{h^2} & -\frac{6}{h} \\ \frac{6}{h} & 2 & -\frac{6}{h} & 4 \end{bmatrix} \tag{5.30}$$

$$\kappa = w_p t_p E_p \left(\zeta^2 + \zeta t_p + \frac{t_p^2}{3} \right)$$

The piezoceramic elemental mass matrix is derived in the same fashion as an ordinary structural element with the exception that the piezoceramic material linear mass density be used instead of the ordinary material density of the structure to which it is bonded.

For structural elements that have piezoceramic material bonded to them, their respective mass and stiffness matrices are given by the simple addition of the beam elemental matrices and the piezoceramic elemental matrices which are then assembled into global mass and stiffness matrices as in the previous section.

$$\begin{aligned} [M]_{element} &= [m]_{beam} + [m]_{piezo} \\ [K]_{element} &= [k]_{beam} + [k]_{piezo} \end{aligned} \tag{5.31}$$

VI. VISIONSERVER CAMERA SYSTEM

The *VisionServer* camera system is a complete hardware and software system designed to meet vision system needs such as real-time control applications. The system locates and tracks passive or active targets and outputs selected data via a digital-to-analog converter and network interface.

Groups of targets can be identified and tracked as individual objects or as bodies. Three targets make up a body and the *VisionServer* can output a body's x,y, and θ values in addition to their rates of change. For a point target, a single LED is used and the system can output x and y translational data only.

The *VisionServer* system is capable of high-speed planer position and orientation measurement of multiple moving objects with sub-pixel resolution on the order of $1/20^{\text{th}}$ of a pixel, which for this setup translates to 0.5 mm accuracy. Under optimal conditions, with an accurate calibration, the system can provide accuracy down to 0.1 mm. The system is also capable of satisfying both real-time modules (*VxWorks*) and supervisory modules (UNIX) concurrently. Some of the basic features include:

- 60 Hz sampling rate for real-time tracking of multiple objects
- Very high resolution (4000:1 or better)
- Optional velocity estimates for all objects

The *VisionServer* hardware consists of a Pulnix TM-440X (CCIR) charged coupled device (CCD) as the sensor, a dedicated Motorola MC68030 microprocessor as

the target architecture, and a Sun SPARC-20 workstation as the host/supervisor architecture.

The CCD camera has an 8mm lens whose viewing angle is approximately 38 degrees and connects directly to the target machine. The camera is capable of sensing either infrared LEDs or reflective tape with spot lighting. The camera must be calibrated for the specific type of light source in order to maintain sub-pixel resolution. The performance tradeoff for the CCD is its height above the plane on which it is measuring the moving objects. As the distance increases, coverage area increases but resolution decreases.

The target architecture is a Heurikon V3D VME-based processor board that has a dedicated Motorola MC68030 microprocessor onboard. The operating system is *VxWorks*, a real-time application-specific operating system. The system processes the digital data from the CCD and converts the signal to a twelve-bit value. The value is then sent to the Xylog XVME-505 16-channel digital-to-analog (D/A) converter card where it is quantized and output as a voltage to the AC-100 analog-to-digital (A/D) converter. The output voltage from the D/A card is limited to ± 10 volts. The sampling rate is fixed at 60 Hz which limits the experimental sampling rate to 30 Hz to avoid aliasing problems.

The host architecture is a Sun SPARC-20 workstation operating SunOS 4.1.3 (UNIX) as its operating system. The host machine contains all the required files and executable code for the target processor, and is connected to the target processor via an internet network adapter card. The host machine also contains two supervisory programs to allow user interface with the *VisionServer* camera system: *StethoScope*, a real-time

graphical monitoring and data collection utility, and *ControlShell*, an object-oriented framework for the real-time system software.

StethoScope is a real-time graphical monitoring and analysis tool that runs in the Sun OpenWindows environment. It allows examination and analysis of the real-time application while it is running. Its powerful multi-window environment enables the user to select specific variables to observe and collect. The data collection utility allows the user to interface with Matlab or MATRIXx and save collected samples in either format.

The *ControlShell* provides a series of execution and data interchange mechanisms that form a framework for building real-time applications. The shell is the primary user interface with the *VisionServer* system. It allows configuration and calibration of the *VisionServer* system software to fit the user's needs. Appendix A contains files necessary to configure the *VisionServer* system. Figure 6.1 shows the block diagram for the hardware setup used for the experimental portion of this thesis.

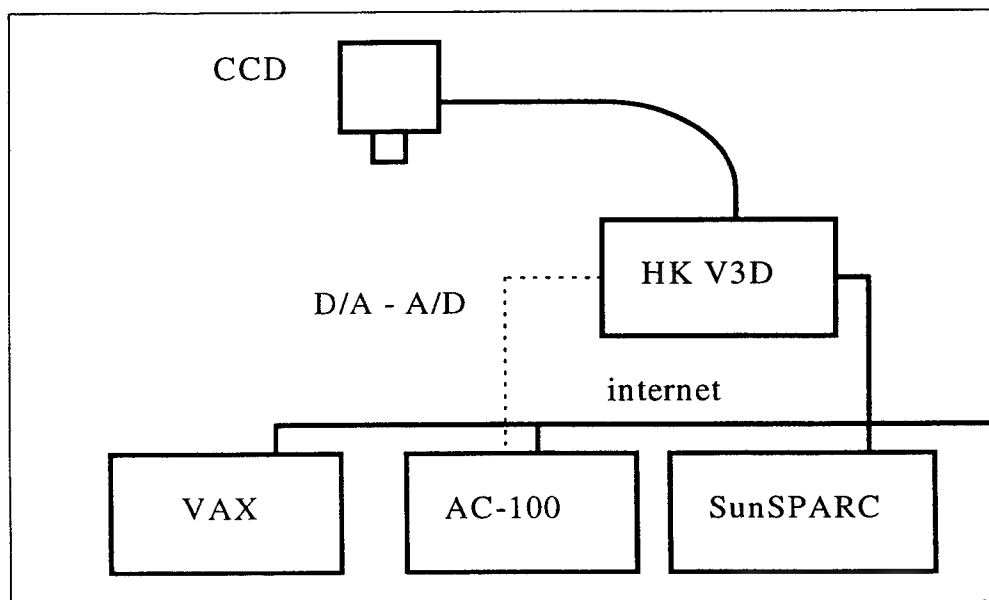


Figure 6.1. *VisionServer* Experimental Setup

VII. ANALYTICAL MODEL

A. FINITE ELEMENT MODEL

The flexible appendage is modeled using the finite element method (FEM). Initially, a twelve element model was used to characterize the system. The twelve element model experienced controllability and observability problems and the order of the model was reduced to a six element model. This process is explained in detail in Chapter III, Section E. The theory in Chapter V is used to create the model shown in Figure 7.1. Elements 1 and 4 are the piezoceramic actuator elements, elements 2 and 5 are the piezoceramic sensor elements, and the VisionServer tracks the Elbow and Tip, both containing three infrared LEDs, respectively.

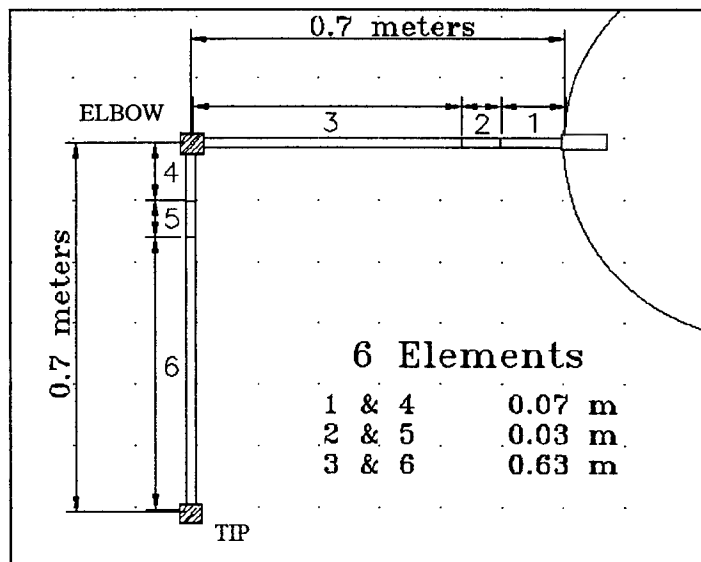


Figure 7.1. Finite Element Model of the FSS Flexible Appendage

Incorporating the piezoelectric theory from Chapter IV into the finite element model, the system state-space matrices (**A**,**B**,**C**, and **D**) were determined [Ref.1]. Appendix B contains the Matlab program (**fem.m**) used to characterize the system along with the respective system matrices. Table 7.1 gives the material properties and parameters for the finite element model used.

7075 T-6 Aluminum Beam			
Quantity	Description	Units	Value
t_b	Beam thickness	meters	1.5875×10^{-3}
w_b	Beam width	meters	0.0254
ρ_b	Beam density	kg/m^3	2800
E_b	Young's Modulus	N/m^2	1.029×10^7
Navy Type II PZT			
Quantity	Description	Units	Value
d_{31}	Lateral strain coefficient	m/V or $Coul/N$	1.8×10^{-10}
E_p	Young's Modulus	N/m^2	6.3×10^{10}
ν	Poisson's ratio	N/A	0.35
D	Absolute permittivity	$Farad/m$ or N/V^2	1.5×10^{-8}

Table 7.1. Model material properties

Using the material properties from Table 7.1 the finite element model produced twelve natural modes of vibration. Table 7.2 gives the values for the natural frequencies and Figures 7.2 and 7.3 give the modeshapes for the first two modes. These two modes are the primary carriers of energy for the structure and it is they that the compensator will be designed to actively control. Appendix C contains the complete set of modeshapes as determined by the finite element model.

Mode	Frequency (Hz)
1	0.2958
2	0.8707
3	11.108
4	28.496
5	45.144
6	102.78
7	278.83
8	341.04
9	1347.7
10	1392.7
11	5284.5
12	5343.0

Table 7.2. Finite Element Model Natural Frequencies

The number of frequencies and modeshapes generally considered accurate from a finite element model is equal to half the number of elements used. In this case, six elements are used and thus the first three modes are considered sufficiently accurate. Using an elementary experimental modal procedure, the first three modes of vibration were determined to be 0.288 Hz , 0.877 Hz, and 9.82 Hz, respectively. This indicates percentage errors for the first three modes of 2.7%, 0.72%, and 13.1 % each.

Since we are concerned with only the first two modes, this model should suffice for the design of the experimental controller.

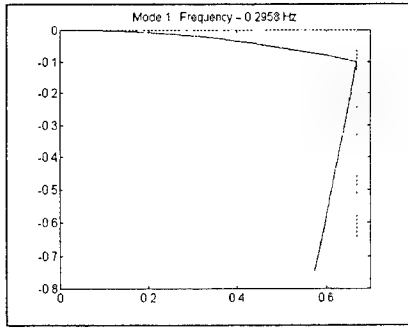


Figure 7.2. Modeshape for first mode

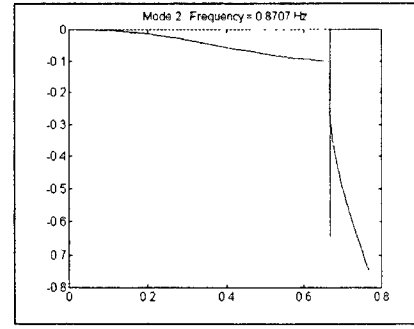


Figure 7.3. Modeshape for second mode

B. SIMULATION RESULTS

The general state-space equations for this system are

$$\dot{\mathbf{x}} = \mathbf{A}\mathbf{x} + \mathbf{B}\mathbf{u} + \mathbf{F}\mathbf{w} \quad (7.1)$$

$$\mathbf{y} = \mathbf{C}\mathbf{x} + \mathbf{v}$$

The system matrix, \mathbf{A} , is a high fidelity twenty-four state model with incorporated structural damping approximating the actual FSS flexible arm assembly. The control matrix, \mathbf{B} , based on equation (5.29) has two independent actuators and is a 24×2 matrix. The sensor matrix, \mathbf{C} , is a 6×24 matrix that contains two piezoceramic sensor outputs and four outputs from an optical infrared *VisionServer* camera system. The piezoceramic outputs are governed by equation (5.29). The *VisionServer* measures the displacements and rotations of the elbow and tip assemblies individually and outputs those four states directly.

The values of \mathbf{Q}_y , the output weighting matrix, and \mathbf{R} , the control weighting matrix, were determined from simulation [Ref. 1] as

$$\mathbf{Q}_y = \begin{bmatrix} 100 & 0 & 0 & 0 & 0 & 0 \\ 0 & 100 & 0 & 0 & 0 & 0 \\ 0 & 0 & 1 & 0 & 0 & 0 \\ 0 & 0 & 0 & 1 & 0 & 0 \\ 0 & 0 & 0 & 0 & 9000 & 0 \\ 0 & 0 & 0 & 0 & 0 & 900000 \end{bmatrix} \quad \mathbf{R} = \begin{bmatrix} 0.1 & 0 \\ 0 & 0.1 \end{bmatrix} \quad (7.2)$$

where the sensor output vector, \mathbf{y} , contains the piezoceramic sensors as the first two elements (volts) and four VisionServer outputs (elbow displacement, elbow rotation, tip displacement, and tip rotation) as the last four elements (meters and radians, respectively) of the output vector. The two control inputs (volts) are the base actuator and the elbow actuator, respectively.

These values kept the control inputs within their limitations of ± 150 volts, the sensors within their limitations of ± 10 volts, minimized the steady state error, and met a 20 second settling time constraint. Figure 7.4 illustrates the simulation results for a typical tip rotational displacement in the time domain, it is representative of all simulation sensor data observed. The upper graph is the open-loop response to a disturbance and the bottom is the LQR controller response to the same disturbance.

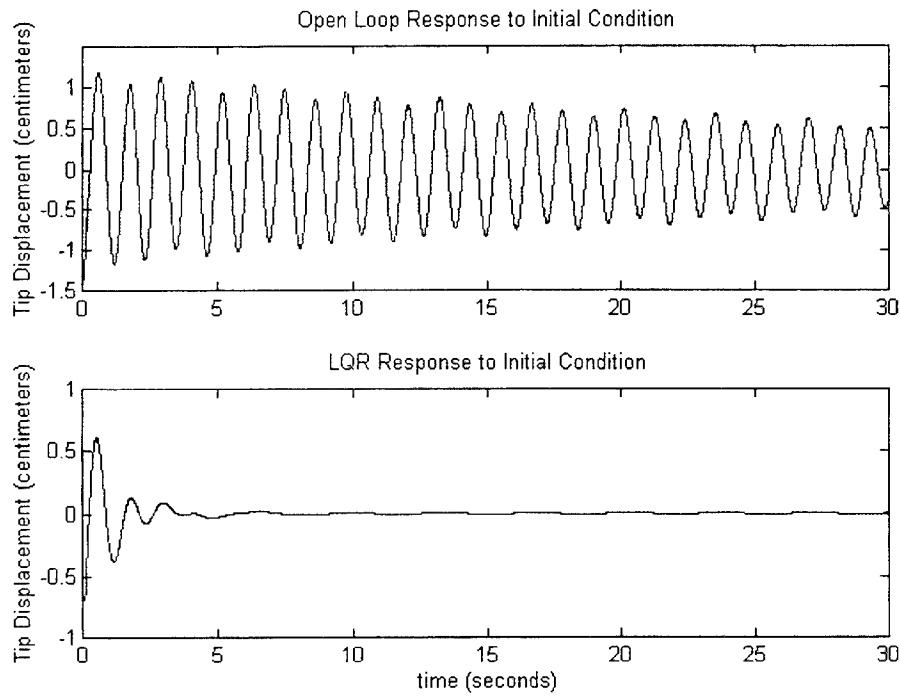


Figure 7.4. Tip Rotational Displacement Initial Condition Response

For the Kalman filter design, the plant uncertainty matrix, F , is the identity matrix and the model uncertainty (W) is approximated at 5%. The sensor process-noise is taken as the squares of component rms noise values (V matrix diagonal elements) from documentation and previous research.

$$W = 0.05[I] \quad V = \begin{bmatrix} 0.0001 & 0 & 0 & 0 & 0 & 0 \\ 0 & 0.0001 & 0 & 0 & 0 & 0 \\ 0 & 0 & 0.00025 & 0 & 0 & 0 \\ 0 & 0 & 0 & 0.002 & 0 & 0 \\ 0 & 0 & 0 & 0 & 0.00025 & 0 \\ 0 & 0 & 0 & 0 & 0 & 0.001 \end{bmatrix} \quad (7.3)$$

A method for determining the performance of the LQG controller is to measure the damping effectiveness for the system. One method for determining the damping from data is the Log Decrement method given by

$$\zeta = \frac{1}{2\pi n} \ln\left(\frac{A_i}{A_f}\right) \quad (7.4)$$

with ζ being the damping ratio, n the number of cycles between measurements, A_i and A_f the initial and final amplitudes, respectively. In order to determine damping, we need to excite one mode at a time. In general, we were able to excite independently only the first two modes. The damping coefficients for the first two modes were determined by simulated excitation of those modes. The results using the log decrement method were 12% [Ref. 1]. Recalling the original damping ratio of 0.4% an increase in damping on the order of 29 times or 2,900% was obtained.

This model was discretized using a Tustin transformation and the values of the system matrices were inserted into the System Build digital controller design on the VAXstation. The next chapter describes the experimental setup followed by the experimental analysis.

VIII. EXPERIMENTAL SETUP

A. OVERVIEW

The Spacecraft Dynamics and Control Laboratory Flexible Spacecraft Simulator (FSS) simulates attitude motion about the pitch axis of a spacecraft. As shown in Figures 8.1 and 8.2 it consists of a single degree-of-freedom rigid central body, representing the spacecraft central body, and a multiple degree-of-freedom flexible appendage, representing an antenna reflector with a flexible support structure.

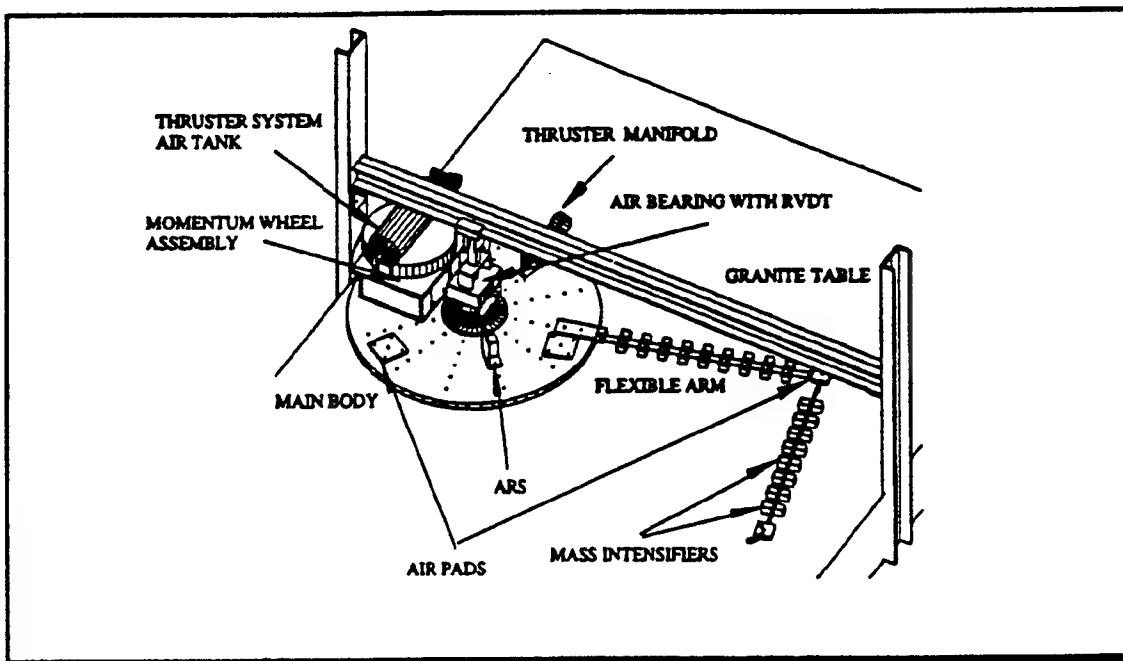


Figure 8.1. NPS Flexible Spacecraft Simulator (FSS)

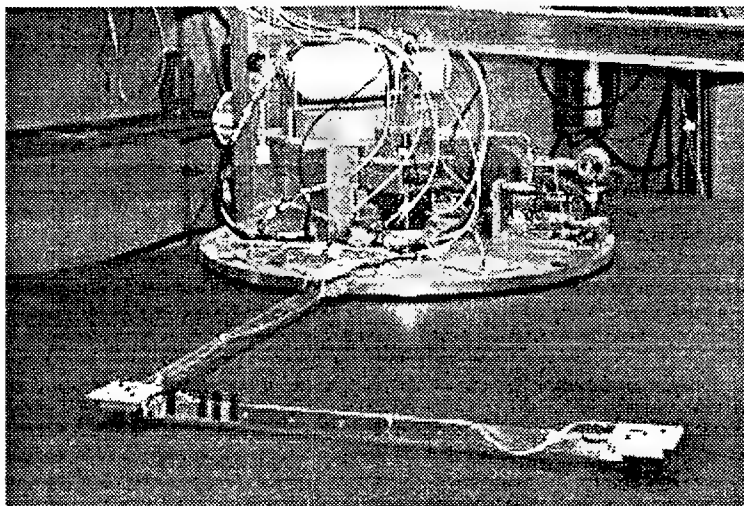


Figure 8.2. NPS FSS Flexible Arm Assembly

Piezoceramic sensors and actuators are used to provide active damping to the flexible support structure. The flexible appendage has two stacked piezoceramic pairs as sensor/actuators. The first pair is located at the base of the arm assembly as shown in Figure 8.3 and the second is located at the base of the forearm near the structure's elbow as in Figure 8.4.

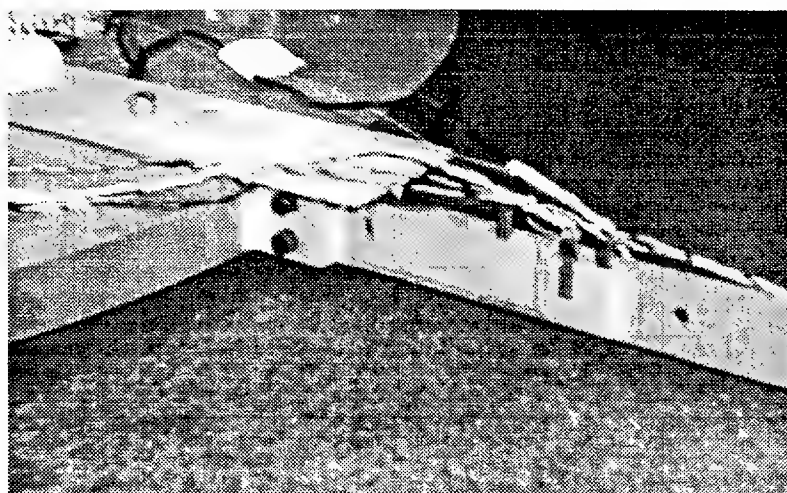


Figure 8.3. Base Sensor/Actuator Pair

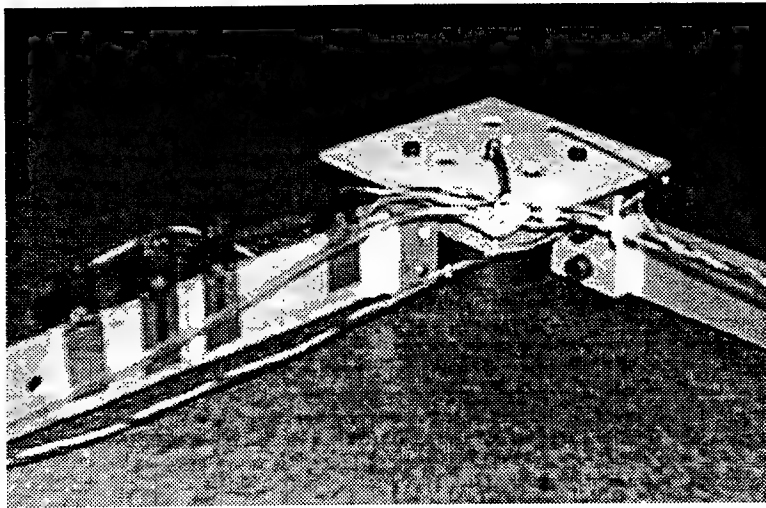


Figure 8.4. Elbow Sensor/Actuator Pair

An overhead infrared camera system is used as a sensor to track designated targets and output their values to the AC-100 real-time control system. Figure 8.5 shows the camera mount for the *VisionServer* system.



Figure 8.5. *VisionServer* Camera (CCD)

The *VisionServer* tracks two groups of three LEDs mounted on the Elbow and Tip. Figures 8.6 and 8.7 are descriptive of the LED layout for the Elbow and Tip bodies.

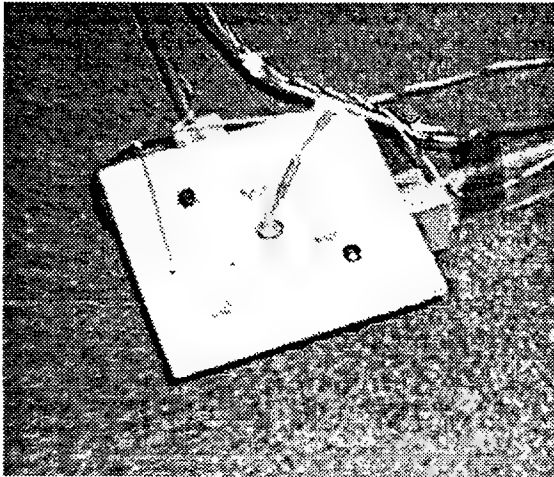


Figure 8.6. Elbow LED Layout

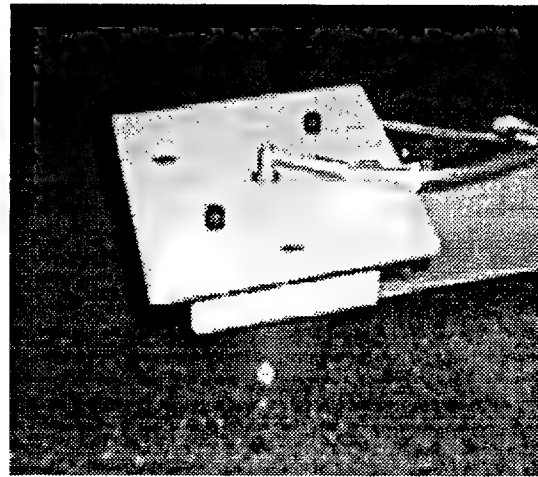


Figure 8.7. Tip LED Layout

The entire system is floated on air pads over a finely ground granite table to simulate a microgravity environment. The central body has two thrusters and a momentum wheel as its actuators. For this experimental verification of a LQG controller, the main body will be fixed to the table and the flexible appendage will be floated and allowed to vibrate freely, and there will be no mass intensifiers on the structure. All disturbances will be created by the software controller in System Build. Figure 8.8 gives an overall view of the VAXstation 3100 and the AC-100 Real-Time Controller.

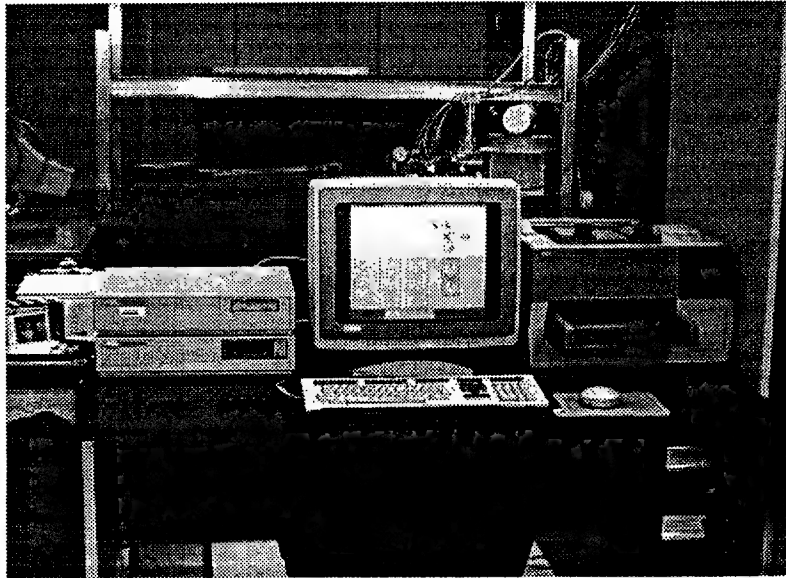


Figure 8.8. Control Workstation Setup for FSS Experiment

B. AC-100 REAL-TIME CONTROLLER SETUP

The AC-100 real-time controller is manufactured by Integrated Systems, Inc. It consists of a host machine and the real-time control processor. The host machine is a VAXstation 3100 that is connected via an internet adapter to the real-time control processor, an Intel 80386 microprocessor. Figure 6.1 shows the block diagram of the hardware connectivity for this experiment.

The AC-100 processor is connected to the experimental apparatus via two A/D converters for the sensor inputs and one D/A converter for the actuator outputs. All D/A and A/D devices are limited to ± 10 volts as inputs and outputs.

The first A/D receives data from the two piezoceramic sensors mounted on each beam of the flexible arm structure. The connections are single-ended connections due to

restrictions on hardware functionality. This condition will introduce noise into the system and must be accounted for in the Kalman estimator.

The second A/D card has the VisionServer inputs, namely the elbow's displacement and rotation, and the tip's displacement and rotation from their respective rest positions. These inputs are also single-ended connections.

The one D/A card connects the digital controller to the two stacked piezoceramic actuators on the structure through a high voltage charge amplifier unit with a calibrated gain of -15. The output signals from the D/A card are limited to ± 10 volts which correspond to a charge amplifier output of ± 150 volts. This voltage is sufficient to actuate the piezoceramics without running the danger of de-poling them.

The digital control system was implemented using MATRIXx, its graphical design tool System Build, and the AC-100 control software Real-Time Monitor (RTMONIT). A block diagram of the complete LQG control system is given in Figure 8.9.

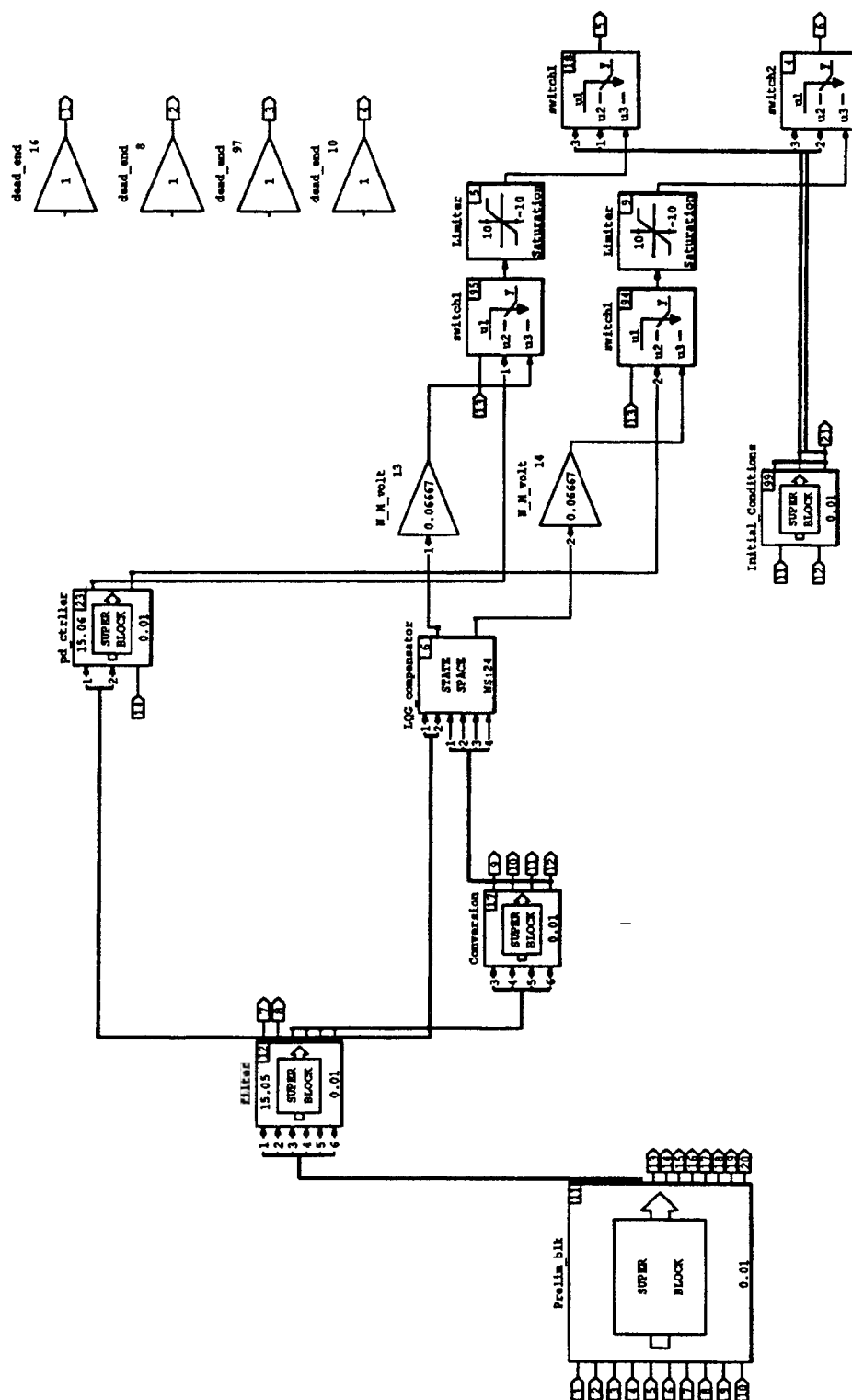


Figure 8.9. System Build Block Diagram For Experimental Controller Verification

The System Build block diagram is transformed to a real-time file (RTF) format, compiled and linked by the C-compiler then uploaded to the AC-100 processor for execution.

C. VISIONSERVER SETUP

The CCD video camera is mounted 1.9 meters above the granite table assembly. It is connected to the 68030 microprocessor running a real-time operating system, *VxWorks*. The twelve bit digital data obtained by the camera is ported out of the 68030 via a digital-to-analog converter card at 60 Hz sampling frequency. The camera's resolution is nominally at the sub-pixel level on the order of $1/20^{\text{th}}$ of a pixel which leads to a camera accuracy of approximately 0.5 mm.

The VisionServer system was calibrated using standard remote control LEDs. The LEDs used for the experiment are much more efficient and have better luminance properties. Thus, the system is not optimally calibrated resulting in a lower accuracy of 0.5 mm instead of the advertised 0.1 mm that the system can produce with an optimal calibration.

The major drawback with the experimental setup is the fact that the signal must travel out of the HK V3D board through the D/A converter along a fifteen foot single-ended cable through an A/D converter into the real time controller, the AC-100. Neither of the converter cards have pre-aliasing filters, thus a fair amount of noise is present in the signal. This fact was taken into account when designing the optimal Kalman observer.

The arm structure has nine LEDs mounted in triplets at the base, elbow, and tip of the flexible structure. Three LEDs make up a body and the *VisionServer* can output a

body's x, y , and θ values in addition to their rates of change. For a point target, a single LED is used and the system can output x and y translational data only.

For this experiment, the base, elbow, and tip are the three bodies used by the *VisionServer* system. Translational and rotational data for each body is output to the AC-100 via the D/A - A/D link. The information necessary for this experiment applies to the elbow and tip of the structure as the base is fixed to the table. Appendix A has the software files necessary to configure the system for this experiment.

IX. EXPERIMENTAL PROCEDURE AND RESULTS

A. BIAS REMOVAL AND COORDINATE TRANSFORMATION

The first part of the experimental procedure is to remove the bias from all sensor inputs and perform a coordinate transformation from the global table coordinate system to the local arm coordinate system.

Bias removal is performed by taking a fifteen second running average of each sensor input and latching the mean value. The mean value is then subtracted out in all subsequent calculations during experimentation. Figures 9.1 and 9.2 are the System Build block diagrams for this procedure.

The next step is to perform a coordinate transformation from global coordinates to local coordinates. The *VisionServer* camera system measures all objects in the global frame of reference. In order to transform the global coordinates to local coordinates the rotation angle must be determined. The angle is taken as the latched value of each body's rotational bias from the *measure_bias* block. This rotates the coordinate system to align with the arm's initial coordinate system and the experiment then begins from rest values.

The combination of both of these processes enables each experimental run to start from zero, which in turn keeps the outputs for the *VisionServer* within the required ± 10 volts and enables the measurement of small displacements and rotations to be lifted above the noise floor.

9-NOV-95

Discrete Super-Block	Sampling Interval	First Sample	Ext.Inputs	Ext.Outputs	Enable
measure_bias	0.0100	0.	10	8	Parent

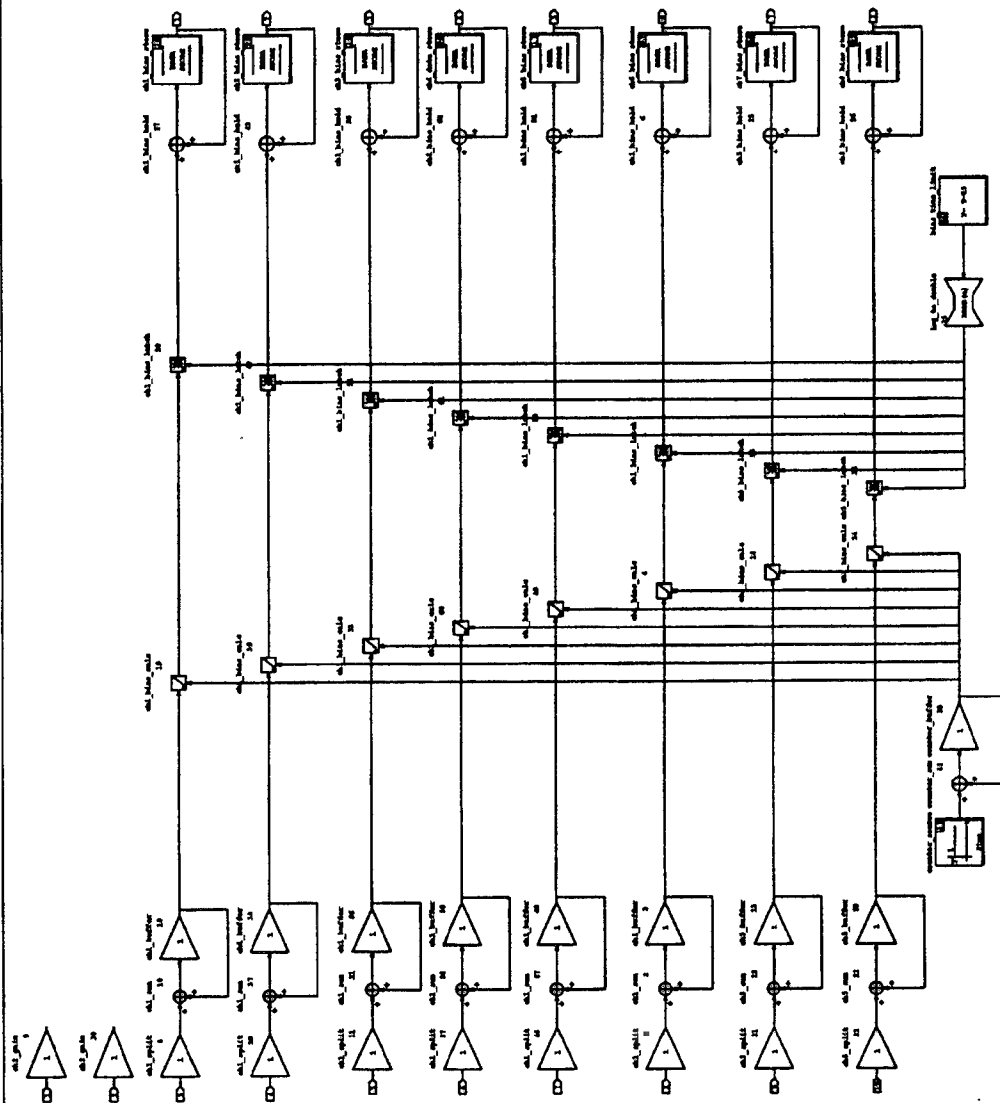


Figure 9.1. Measurement of Sensor Bias Block Diagram

9-NOV-95

Discrete Super-Block	Sampling Interval	First Sample	Ext. Inputs	Ext. Outputs	Enable
Prelim blk	0.0100	0.	10	14	Parent

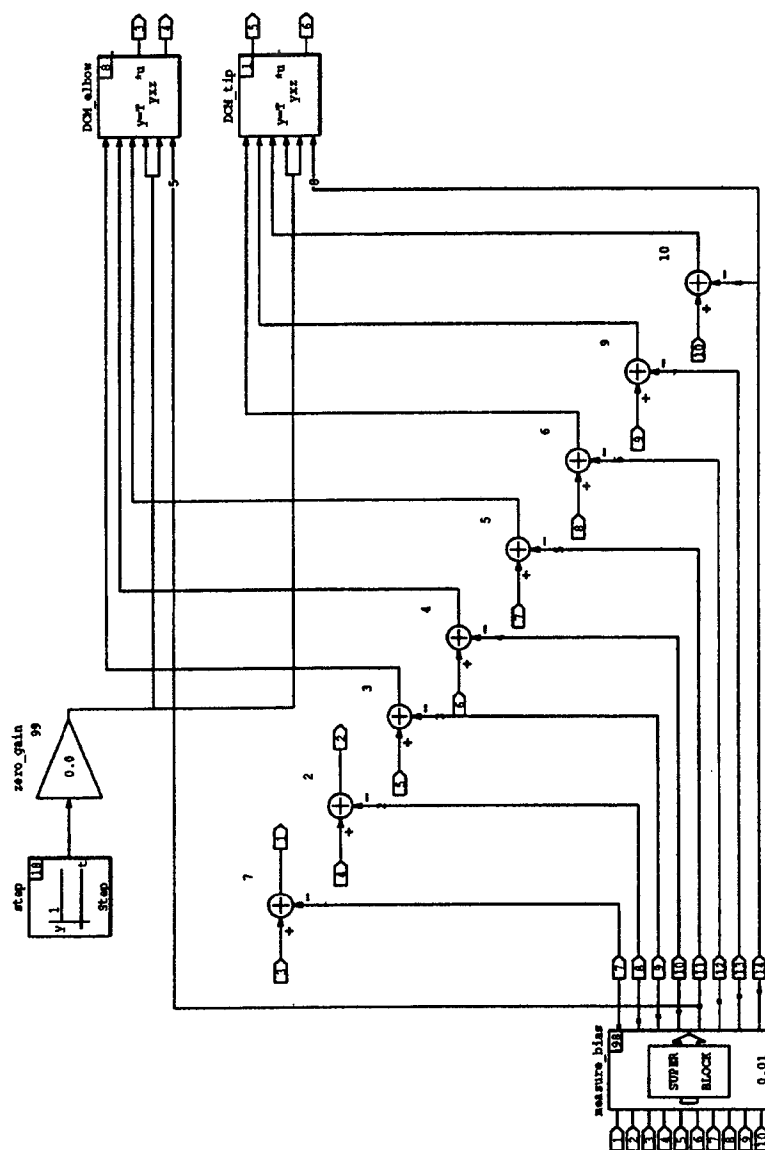


Figure 9.2. Preliminary Block Diagram for Experimental Data Collection

B. FILTERING

Following the coordinate transformation, the signals are passed through a second-order low pass filter (LPF) to eliminate noise and high frequency components. The value for the cutoff frequency was determined to be 2 Hz. Any higher cutoff frequency resulted in large amounts of noise getting into the system. The discrete second-order infinite impulse response filter (IIR) state-space equation is given as follows

$$\begin{aligned} \begin{Bmatrix} y_{n+1} \\ y_{n+2} \end{Bmatrix} &= \begin{bmatrix} 1.823 & -0.837 \\ 1 & 0 \end{bmatrix} \begin{Bmatrix} y_n \\ y_{n+1} \end{Bmatrix} + \begin{Bmatrix} 0.004 \\ 0 \end{Bmatrix} X_n \\ Y_n &= [3.823 \quad 0.163] \begin{Bmatrix} y_n \\ y_{n+1} \end{Bmatrix} + [0.004] X_n \end{aligned} \tag{9.1}$$

with X_n being the input and Y_n being the output of the discrete filter. Using a second-order low-pass filter minimized the associated time delay that accompanies such devices. Since the maximum frequency we are interested in is 0.87 Hz, the time delay is negligible as compared to the sampling frequency of 100 Hz.

C. INITIAL CONDITION RESPONSE

The initial condition is created by the piezoceramic actuators themselves. The actuators are excited for two types of responses, single-mode and multiple-mode responses. Figure 9.3 illustrates the experimental setup for the initial condition block. The two frequencies used are the first and second harmonic frequencies. The logic blocks enable the initial condition input for a ten second period between bias removal and the controller actuation.

9-NOV-95

Discrete Super-Block	Sampling Interval	First Sample	Ext. Inputs	Ext. Outputs	Enable
Initial Conditions	0.0100	0.	2	3	Parent

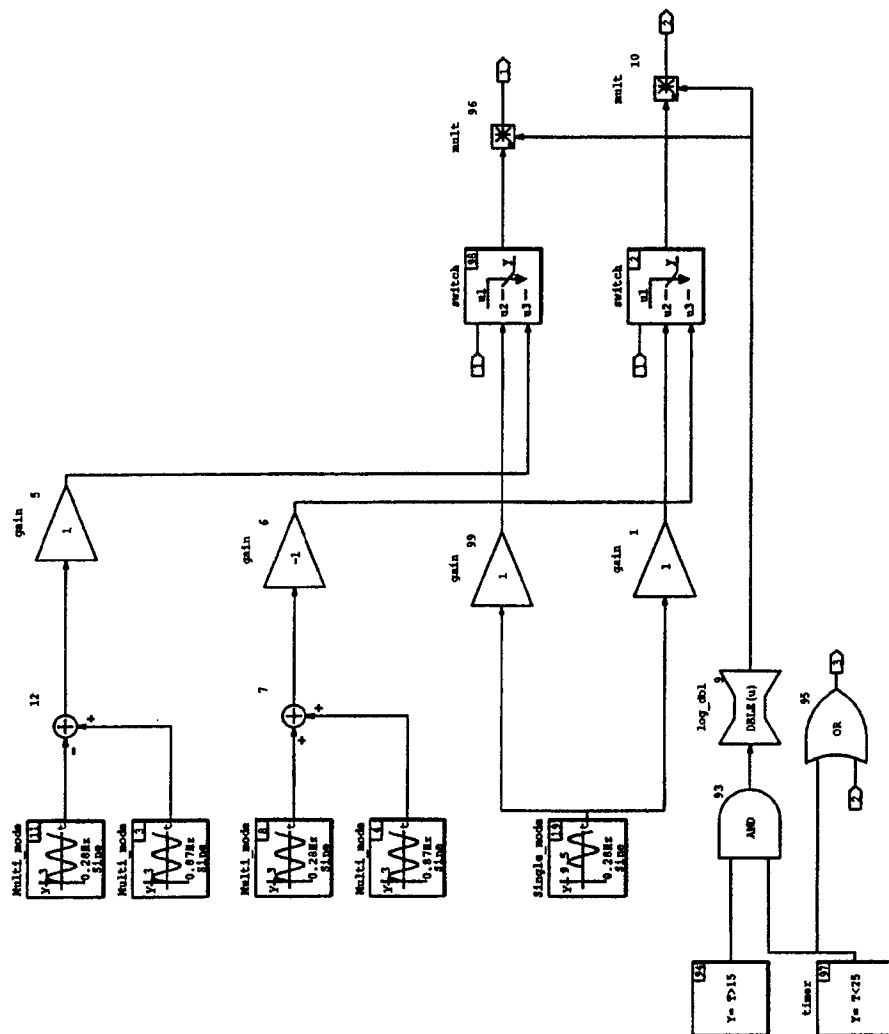


Figure 9.3. Initial Condition Control Block Diagram

The main desire for the initial condition system is reproducibility. Figure 9.4 is a illustration of two test runs plotted on top of each other. The error between the two subsequent open-loop tests is experimentally determined to be 2.7%. The absolute value of the difference between the two runs was determined and then averaged to give the nominal error.

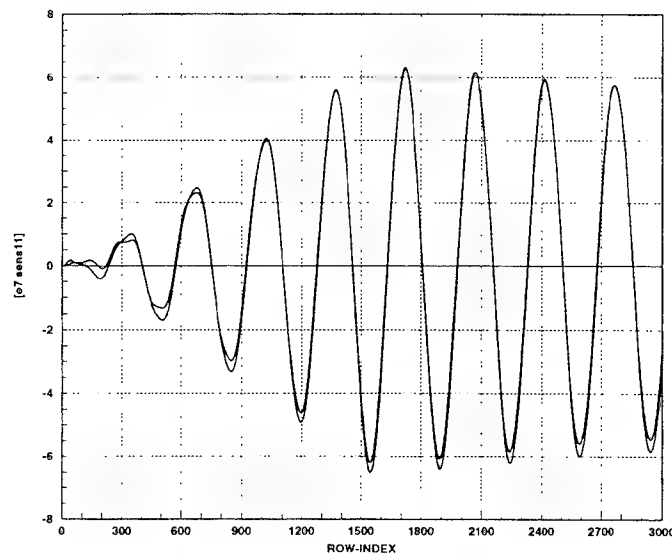


Figure 9.4. Reproducibility Error Test

D. ESTIMATOR VERIFICATION

Next, we must verify that the estimator derived from [Ref. 1] is effective in the real-time implementation. The system is excited as per the initial condition block and then the outputs are compared. Providing the states are being estimated properly, this would indicate that the LQG controller should be effective. Once the estimator is verified the

next phase is the controller testing phase. Figures 9.5 and 9.6 show the filtered sensor outputs, tip displacement and rotation, from the *VisionServer* sensor plotted with their estimated values.

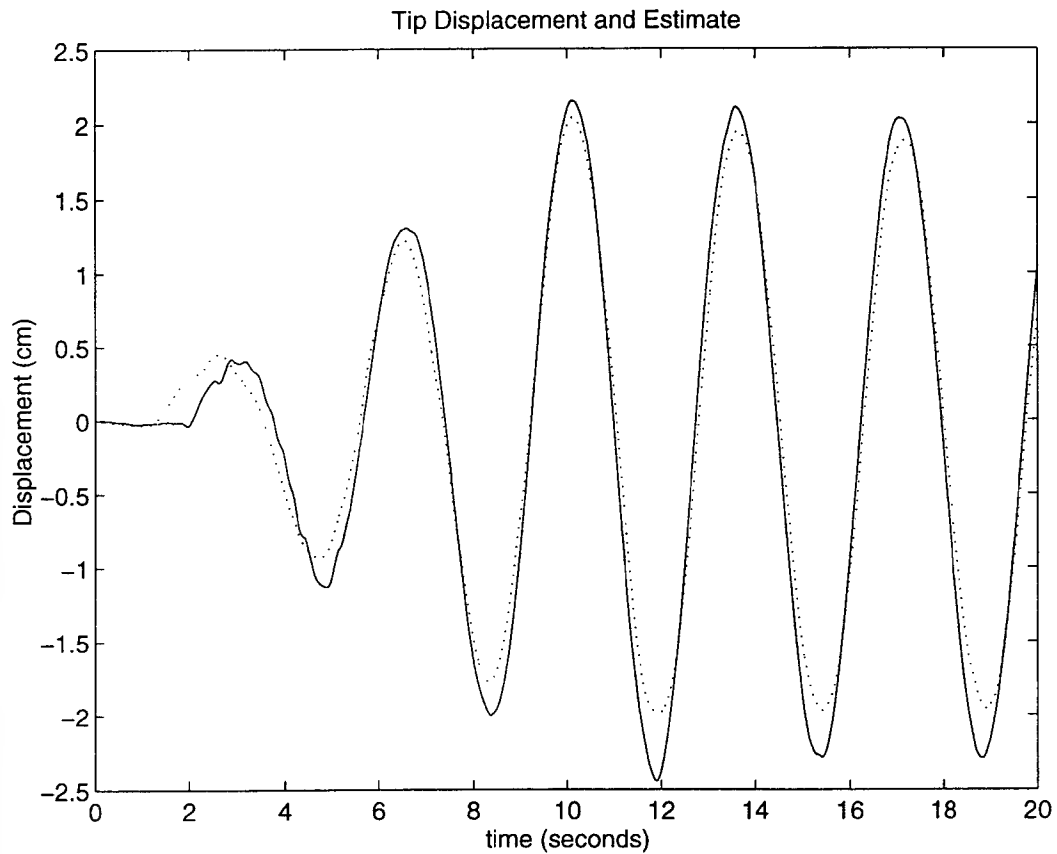


Figure 9.5. Tip Displacement (—) and Estimate (.....)

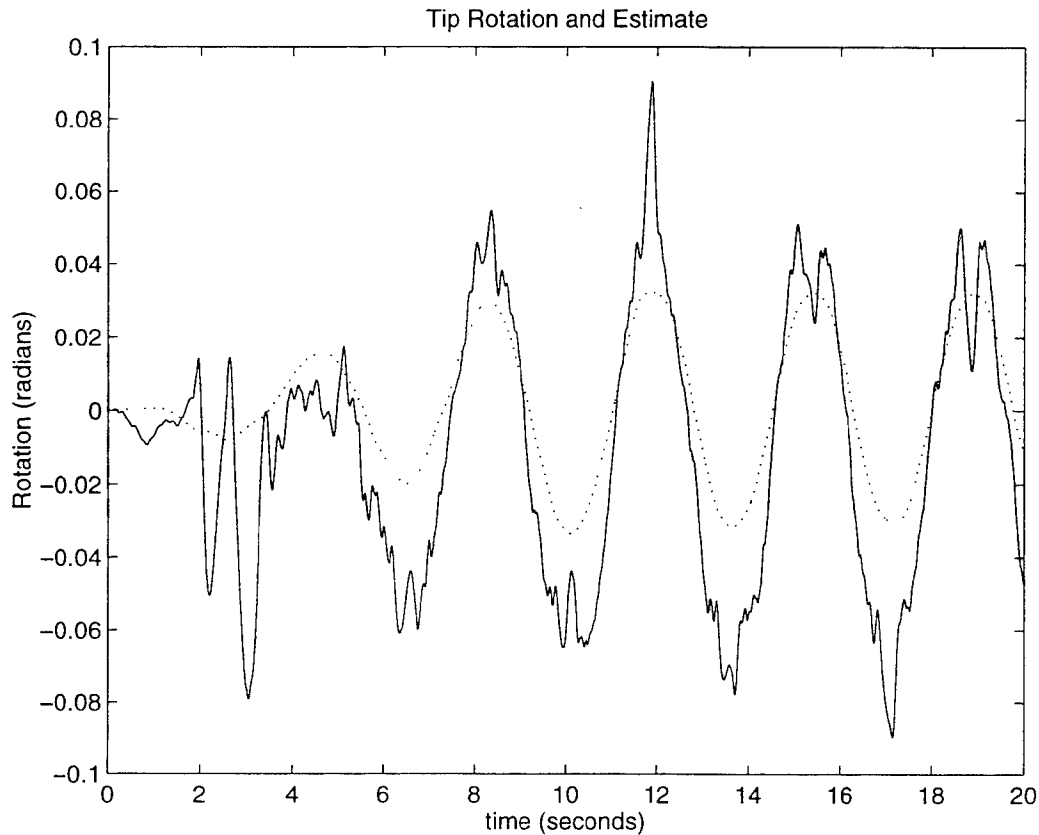


Figure 9.6. Tip Rotation (—) and Estimate (.....)

From the plots it can be seen that the estimator not only estimates the states well, but smoothes out the response as well.

E. CONTROLLER TESTING AND EVALUATION

There are two control types to be tested and compared: the LQG controller from [Ref. 1] and a Positive Position Feedback (PPF) coupled with velocity feedback.

One of the first methods employed to damp the flexible appendage is positive position feedback (PPF). In order to implement this control law on the FSS, it is modeled as a second order system:

$$\ddot{e}_a + 2\zeta_a \omega_a \dot{e}_a + \omega_a^2 e_a = -\omega_a^2 k e_s \quad (9.2)$$

e_a is the actuator applied voltage

e_s is the sensor sensed voltage

ζ_a is the actuator damping ratio

ω_a is the actuator frequency

k is the actuator gain

By setting the actuator frequency equal to the structure fundamental frequency, a 90° phase shift is attained in the region where $\omega_a / \omega_{n1} = 1$. Figure 9.7 illustrates that the effect of this type of compensation is an active damping region in the area of $\omega_a / \omega_{n1} = 1$ with active stiffness for frequencies above this region and active flexibility in the frequencies below this region. Thus it is important to set the actuator frequency at the fundamental structural frequency to avoid an increase in flexible mode strength for lower frequencies.

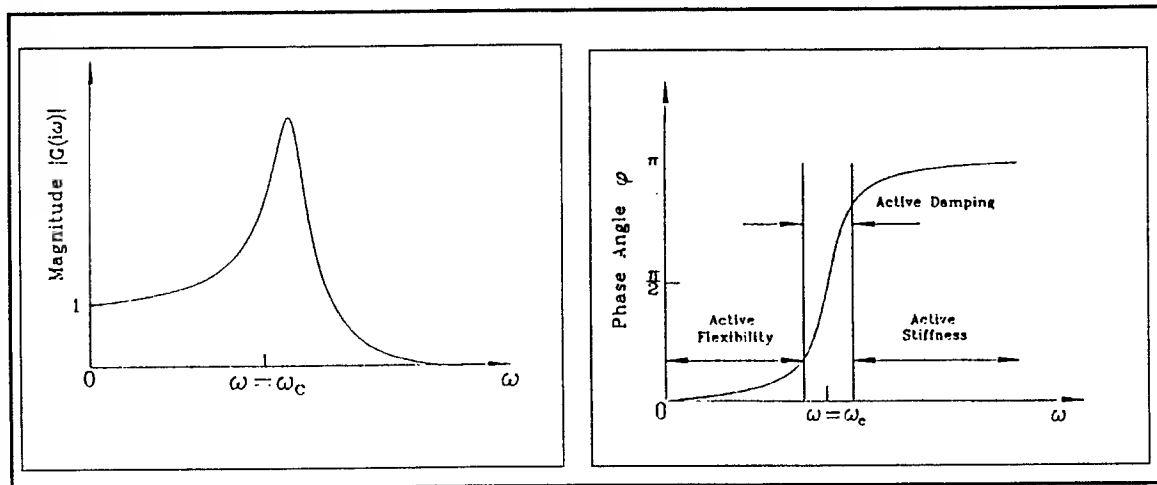


Figure 9.7. Positive Position Feedback Control Theory

Since the PPF controller is effective only for the controller frequency, it is useful to augment PPF with another form of feedback control. Velocity, or derivative, feedback is a simple and effective form of feedback control. The use of velocity feedback increases the effectiveness of the PPF controller by adding damping for all frequencies.

$$e_a = k_v \dot{e}_s \quad (9.3)$$

Figures 9.8 and 9.9 are the experimental results from testing the PPF/Velocity controller using the piezoceramic sensors as the source for the actuator. The targeted mode is the fundamental frequency, 0.288 Hz. The PPF gain is 4 and the Velocity gain is 0.4.

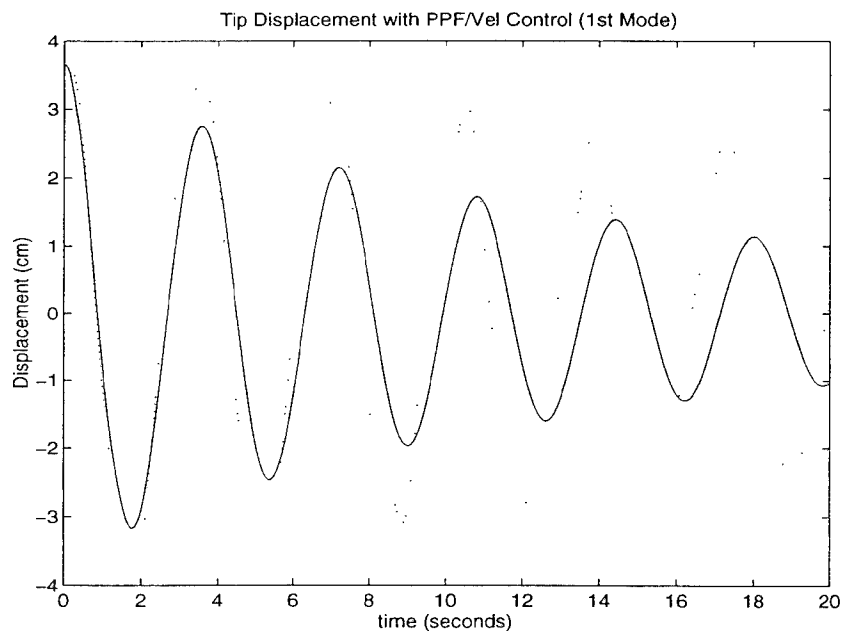
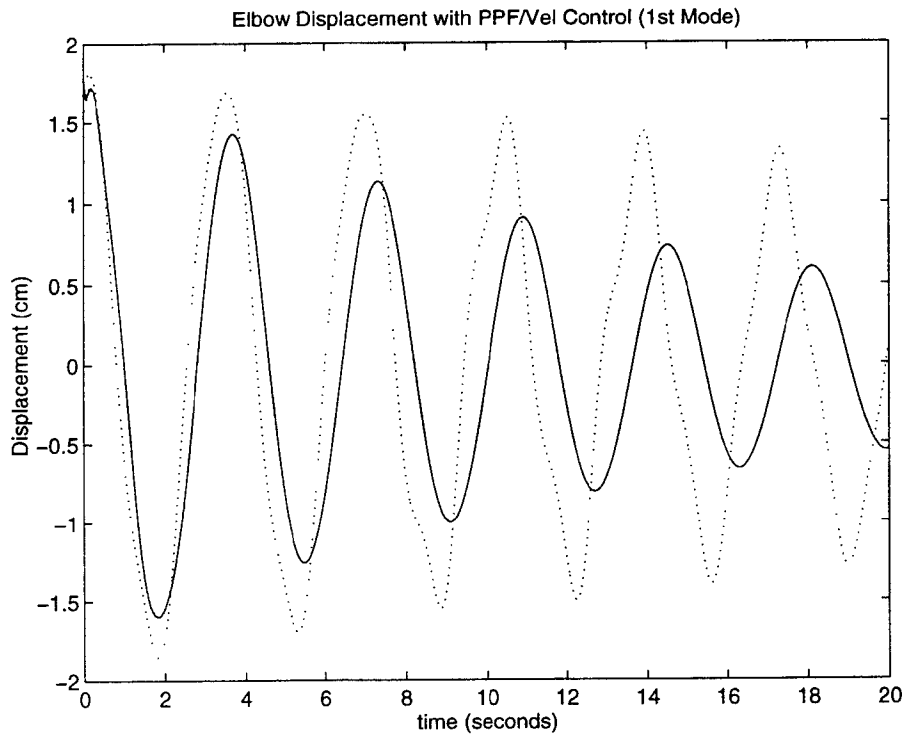


Figure 9.8. PPF Control for Single-Mode Response, Tip Displacement
Damped (—) and Undamped (.....)



**Figure 9.9. PPF Control for Single-Mode Response, Elbow Displacement
Damped (—) and Undamped (.....)**

It is evident that the response is well damped, yet the actuators have only low control authority over the fundamental mode which results in an increased settling time for the system.

Figures 9.10 and 9.11, show the PPF/Velocity response to a multi-mode disturbance, the targeted modes are the fundamental and second harmonic, 0.917 Hz. The actuators damp out the higher modes quickly but again are limited in control authority over the fundamental mode, the gains are the same as those in the single mode.

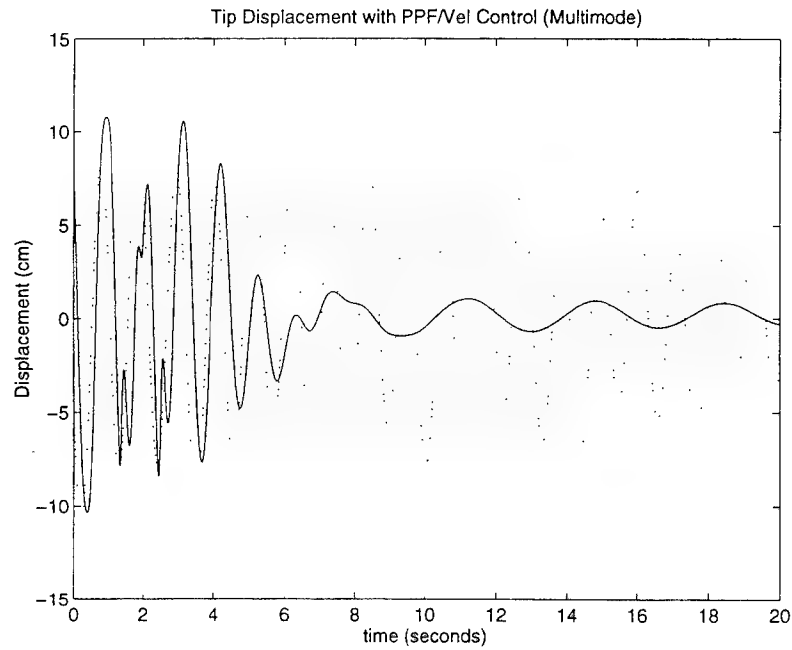


Figure 9.10 PPF Control for Multi-Mode Response, Tip Displacement
Damped (—) and Undamped (.....)

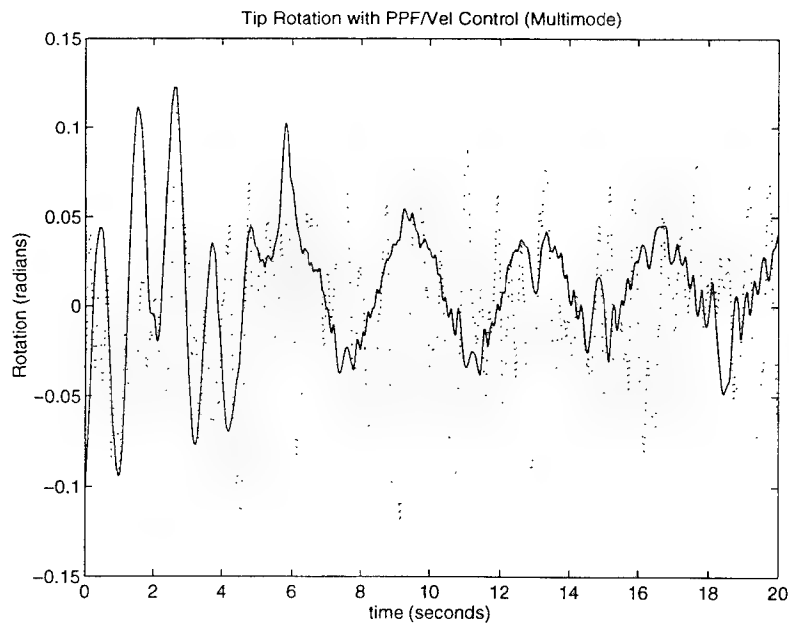


Figure 9.11 PPF Control for Multi-Mode Response, Tip Rotation
Damped (—) and Undamped (.....)

Next, it is desirable to compare the piezoceramic sensors performance with the *VisionServer* camera system performance. The two displacement inputs (tip and elbow) are connected to the PPF/Velocity feedback controller and Figures 9.12 and 9.13 show the result.

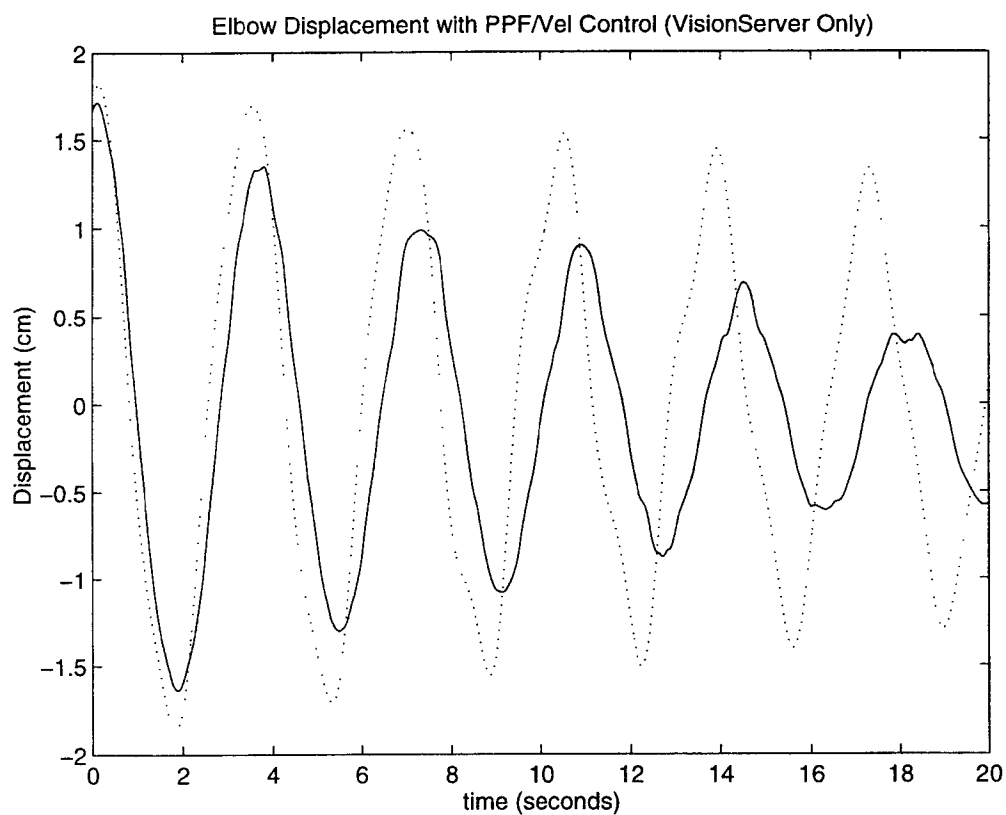


Figure 9.12. PPF Control for Single-Mode Response, VisionServer Input Only
Damped (—) and Undamped (.....)

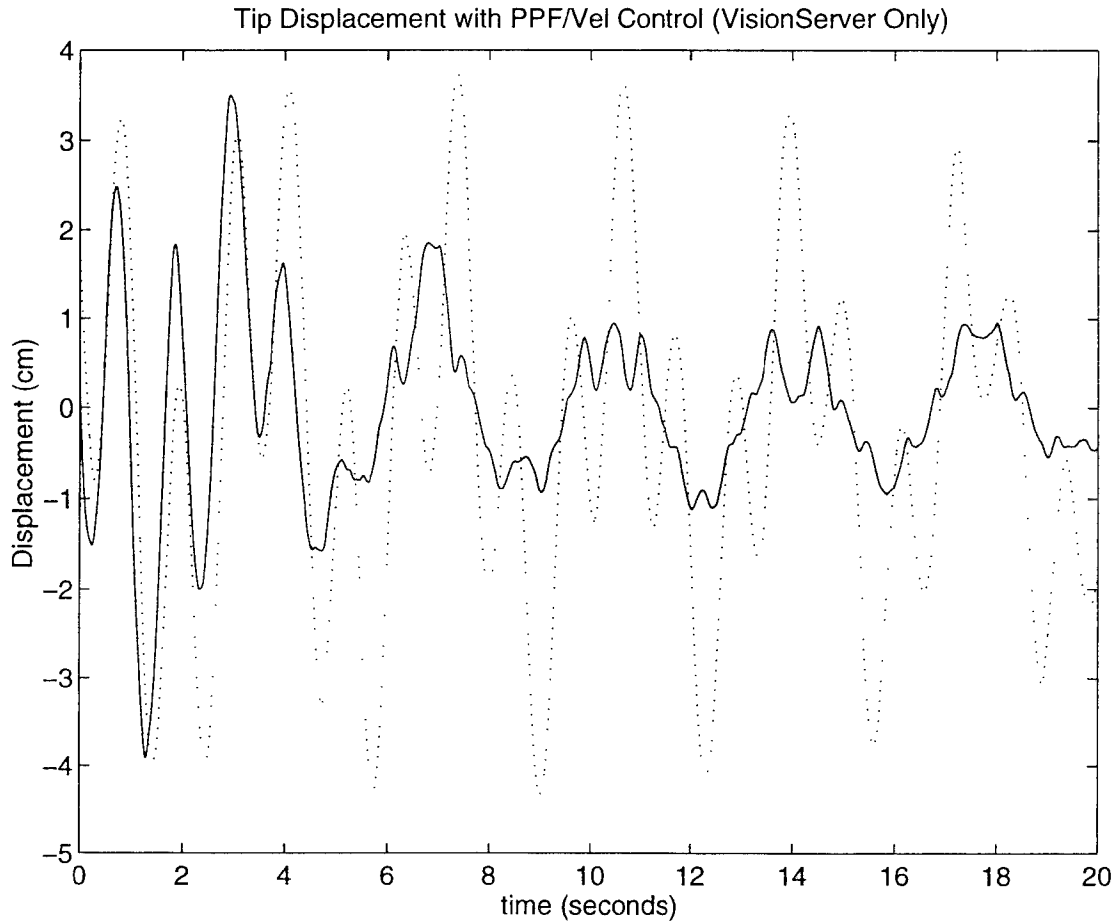
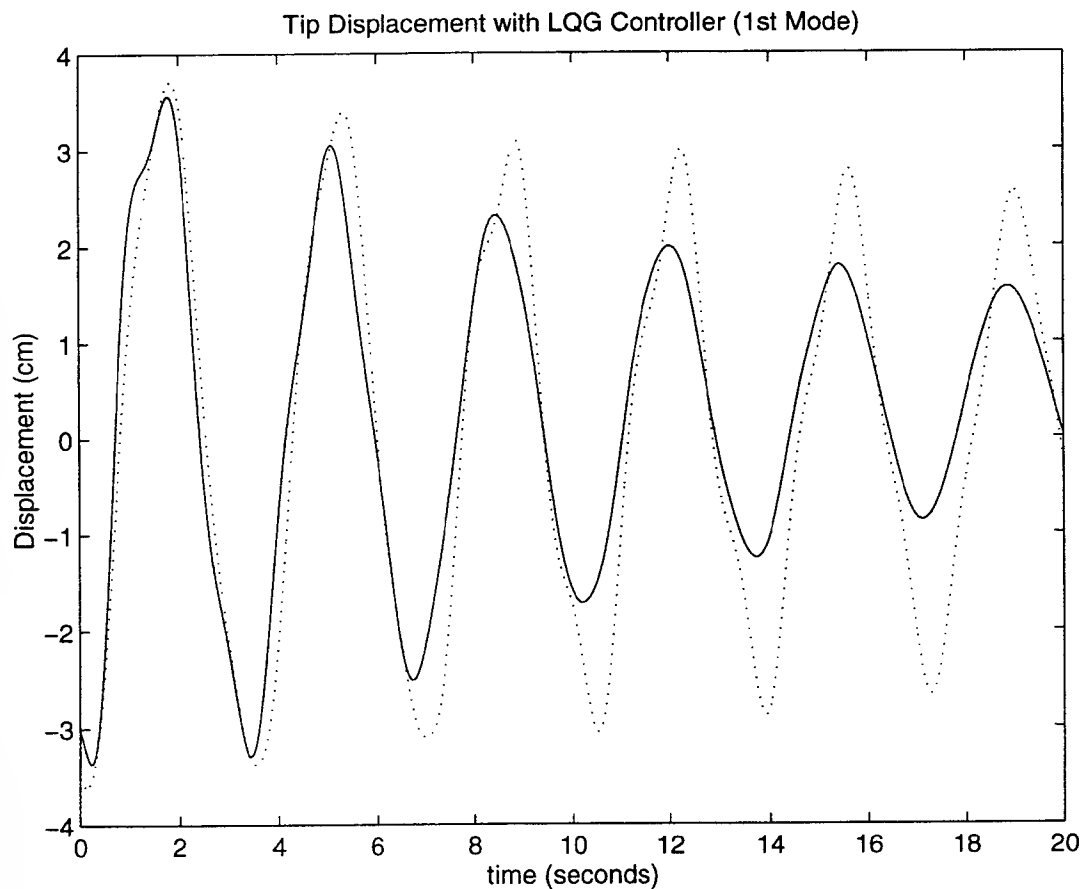


Figure 9.13. Tip PPF Control for Multi-Mode Response, VisionServer Input Only
Damped (—) and Undamped (.....)

The control with the *VisionServer* inputs is not as robust as that with the piezoceramic sensor inputs. This is due to the fact that the raw *VisionServer* inputs are very noisy and after filtering, lose some of their gain. This leads to smaller inputs from the sensors thus less control authority.

The final procedure will be to test the LQG controller and compare the results with the PPF/Velocity Feedback values. The LQG controller is designed for all the sensors inputs to be available for processing. The LQG controller can be expected to be more

sensitive to parameter variations since the assumptions, such as Gaussian noise, in its design [Ref. 1] do not hold true in real-time. The results given by the estimator indicate that the controller should work, but might not be as robust as designed. Figures 9.14 and 9.15 show responses to the LQG controller.



**Figure 9.14. LQG Control for Single-Mode Response, Tip Displacement
Damped (—) and Undamped (.....)**

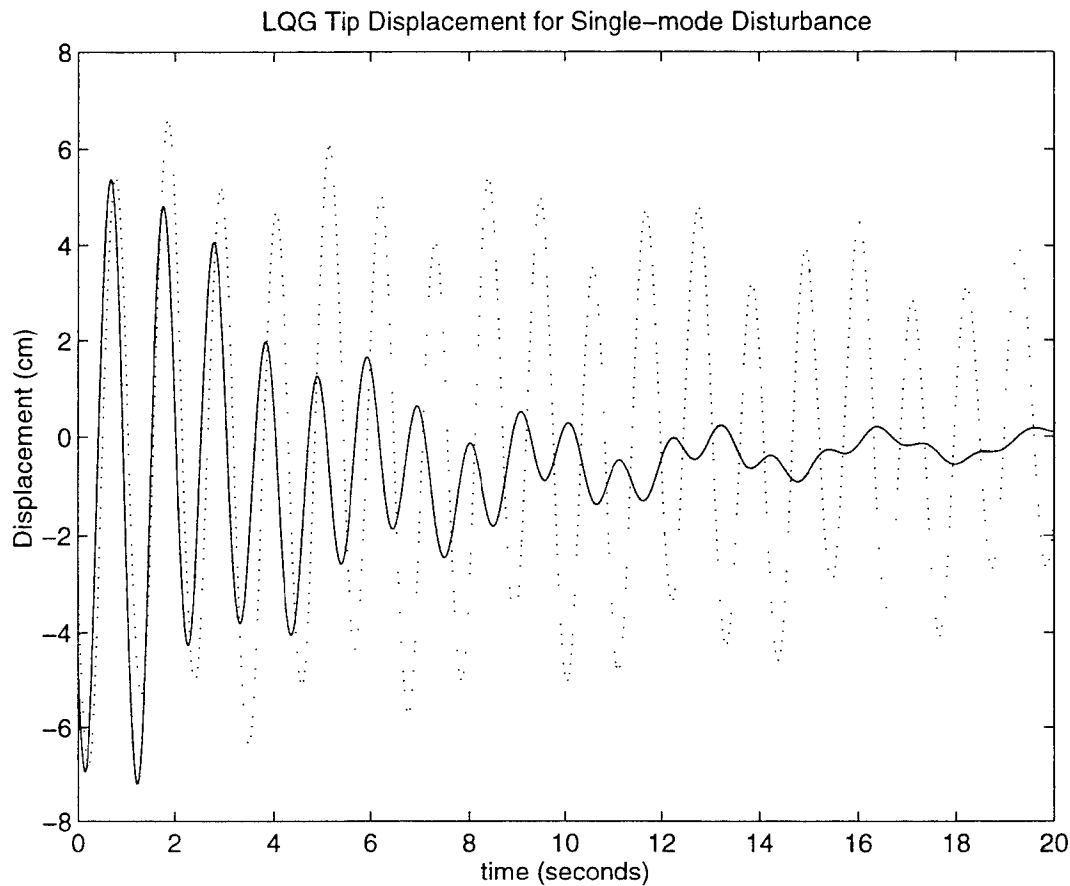


Figure 9.15. LQG Control for Multi-Mode Response, Tip Displacement
Damped (——) and Undamped (.....)

As indicated, the response is satisfactory, but not optimal. The PPF/Velocity controller is comparable if not better in single-mode disturbance rejection. The LQG controller is still an effective control scheme, but more so in multi-mode control scheme. The LQG controller can be better optimized using advanced design techniques such as Loop Transfer Recovery to recover lost robustness and attempt to regain as much control authority as possible.

F. DAMPING SUMMARY

Table 9.1 shows the damping ratios as determined by the log decrement method (Eqn. 7.4) from the experimental results. These results indicate a significant increase in damping by both control schemes with the PPF/Velocity behaving slightly better than the LQG controller. Employing Loop Transfer Recovery might add to the performance of the optimal controller.

	No Control	LQG	PPF/Velocity
Fundamental mode	0.004	0.0367	0.0387
Second mode	0.004	0.0678	0.0701

Table 9.1. Damping Ratios for LQG and PPF/Velocity Feedback Control

X. CONCLUSIONS AND RECOMMENDATIONS

A. SUMMARY

This thesis presents the experimental verification of an optimal controller for a flexible structure model and experiment using Linear Quadratic Gaussian techniques with piezoceramic actuators and sensors and an optical *VisionServer* camera sensor system. The LQG design was an effective controller for the flexible structure as was the PPF/Velocity feedback controller. Both systems required a low pass filter in the loop to reject high frequency noise.

B. CONCLUSIONS

The LQG controller design from [Ref. 1] was implemented and compared with a PPF/Velocity feedback controller. The LQG controller met design specifications but was not as robust as the simulation results predicted [Ref. 1]. The PPF/Velocity controller was very effective with single-mode disturbance rejection and showed limited capability for multi-mode excitations. The LQG controller was effective in damping all excitations but not as effective as the PPF/Velocity controller with single-mode control. The response of the system is limited by the fact that the actuators have low control authority. This is a factor in all controller implementations.

The state estimator is an addition to the system, it performs satisfactorily in estimating the states, and it smoothes out the *VisionServer* inputs.

The *VisionServer* is connected to the controller through two unfiltered digital-analog devices which leads to an extraordinary amount of noise. The raw data input from

the *VisionServer* system is unusable for control applications without a filter or estimator in the loop. The single-ended connections add to the noise problem, a differential connection scheme would minimize noise input to the system through common-mode rejection.

In the simulation results, the damping was increased to 12% [Ref. 1], for the experimental results damping was determined to be on the order of 4% for the fundamental mode, and 7% for the second mode. The differences in the results can be attributed to the estimator performance in real-time.

C. RECOMMENDATIONS

For the controller, the next step is to optimize the LQG design by using advanced design techniques such as Loop Transfer Recovery and μ -analysis to maximize the robustness. Optimal H_∞ control techniques may also prove advantageous for this type of structural control application.

For spacecraft implementation, it is desirable to float the entire FSS and observe the interaction between the attitude controller and the flexible structure controller during slew maneuvering. Isolating the appendage tip from inherent spacecraft vibrations is an area of great interest and is a good follow-on to this work as well.

The *VisionServer* system needs to be connected to the controller by differential connections in order to minimize the noise introduced into the system. The *VisionServer* system software can be modified to measure in local coordinates rather than the global coordinates and thus give a greater dynamic range to the sensor.

REFERENCES

1. Harrington, W., "Optimal Linear Quadratic Gaussian Controller Design for a Flexible-Spacecraft Simulator", Master's Thesis, Naval Postgraduate School, December 1995.
2. Friedland, B., *Control System Design*, McGraw-Hill, New York, 1986.
3. Franklin, G., Powell, J., and Emami-Naeini, A., *Feedback Control of Dynamic Systems*, Chapter 7, Addison-Wesley, Menlo Park, CA, 1994.
4. Z. Chaudhry and C. Rogers, Actuators for Smart Structures, *Fiber Optic Smart Structures*, pp. 497-505, Wiley, New York, 1995.
5. B. Jaffe, R. S. Roth, and S. Marzullo, Piezoelectric Properties of Lead Zirconate-Lead Titanate Solid Solution Ceramics, *Journal of Applied Physics* **25**, 809-810 (1954).
6. Meirovitch, L., *Elements of Vibration Analysis*, pp. 300-312, McGraw-Hill, New York, 1986.
7. Real Time Innovations, Inc., VisionServer Real-Time Vision System, User's Guide, 1992.
8. Shahian, B. and Hassul, M., *Control System Design Using Matlab*, Prentice-Hall, Englewood Cliffs, NJ, 1993.

APPENDIX A

VISIONSERVER SETUP AND SOFTWARE

The setup for the VisionServer system is as follows:

1. Ensure the Internet cables are connected between the target machine (**wfft**) and the host machine (**voyager**). Also ensure the serial connection between the two are connected in case that venue is to be used.
2. Turn on **wfft**, this should suffice and the system should come up and boot automatically. If there is a problem, check that **wfft** has **rsh** (remote shell login capability) access to **voyager**. This can be verified with the system administrator. If that is not the problem, access the boot procedure via the serial connection (**kermit**).

The documentation for the boot procedure is contained in the *VxWorks* Reference Guide.

3. The system should now be up and running. Provided the D/A hookup is connected and LEDs are visible to the camera, data should be streaming out the port. We can now access the *ControlShell* and the *StethoScope* applications.
4. *StethoScope*:

The host computer must be a Sun and running *OpenWindows*. Type **scope wfft &** and a control window should appear on the screen. A status line in the box will let you know that the system is connected to **wfft**. For help on this application, click on the **Help...** icon and an index of man pages will be brought up. To get a Plot window, click on the **View** icon and a plot window will be brought up as well. Within the plot window, right-clicking on the **Signals** arrow will allow you to choose which

signals you want to observe. The data from the signals is near real-time and can be copied to a MATRIXx format or Matlab format for further analysis. The help pages have the procedure for capturing data.

5. *ControlShell*:

To access the *ControlShell*, from a **xterm** window, type **rlogin wfft**, the prompt should be

VxWorks (VisionServer) ->

Enter the command **cs** and the prompt will show

ControlShell ->

You are now in the *ControlShell* application. Hit the Enter key and the menu will pop up for you.. The primary applets you will be concerned with are the

PointGrabber, vision, bodymanager, and scope.

The **PointGrabber** contains two major commands: **a2d** and **threshold**. The nominal values for these are 78 and 180, respectively. By varying these values, the threshold level for the amount of light (IR) and the maximum level of light to saturate the conversion can be optimized. The rule of thumb is to have at least 100 units separation and as high a value for the **a2d** as possible (255 max, recommend no higher than 220).

The **vision** topic allows user control of the tracked targets. To lose all targets enter **vL** (vision Lose), to load all targets **vl -1 n n** (vision load all no velocities no metric units) and to display the targets on the terminal **vd** (vision display).

The bodymanager allow you to maintain the tracking options for bodies. The topic of importance is the **tolerance**. This command enables the user to set the minimum tolerance between two targets for identifying bodies. If a target falls out of this range, it is assumed to be a separate point target.

The scope option allows one to clear off the scope Signals board. By using the **scU** (scope Unload) and **point** commands, the bodies will be the only signals tracked.

Setup Files

The following setup files are read in by the VisionServer system upon initialization:

setup

```
# NPGS setup file.
#
# This setup file causes the vision system to report the location of bodies
# defined in dfe/npgs.dfe to be output to the D/A.
#
# modification history
# -----
# RTI,05oct92,sas Written.
#
#
#####
# Set up the vision system
#
menu read setup.vision

#####
# Read the data flow specification.
#
data read dfe/npgs.dfe
#
#
#####
# Describe the objects
#
menu read setup.describe

#####
# Set up the execution list
#
menu read setup.exe
```

```
#
xecute go
logout
```

setup.vision

```
#####
#
# Set up the vision system (should be the same as pgrabber/setup)
vision rate 1
vision Lose
Frame xecute go
PointGrabber interruptEnable
```

```
#
#####
```

```
#
# Customize it for the ambient conditions
#
```

```
#Pb
PointGrabber threshold 0 78
PointGrabber a2d 0 180
PointGrabber PixelSeparation 2.27
body tolerance 0.003
body inconsistent 0.011
vision verbose 0
```

Note: You can set all ControlShell commands you want in this file.

```
#
# 6Hz observer:
ox 0.5872 16.1893
oy 0.5872 16.1893
ot 0.5872 16.1893
#
#
# Stop VisionServer scope sampling (cuz the controller will do it)
list disable Frame 5000000
```

```
#
PointGrabber heights 0 1.924
PointGrabber correct
0
```

Note: These are the calibration coefficients

```
0.0018
0.0025
0.3287
0.0001
0.0001
-0.0025
-0.0002
0.0017
-0.0001
0.6191
-0.0000
0.0000
0.0028
0.0019
```

-0.0003
0.3269
0.0019
0.0001
0.0024
0.4976

npgs.dfe

This file is where you define you bodies and points.

```
# npgs.dfe      \- data flow system description
#
# modification history
# -----
# TestObject,05oct92,sas  Written.
# Base,Elbow,and Tip added, 03Nov95,wbh Written.
```

#

#

#

attach: npgs

#

Base, body at flexible arm/rigid body interface

CSMat: BasePos 3

x	m	0
y	m	0
theta	rad	0

CSMat: BaseVel 3

x	m/sec	0
y	m/sec	0
theta	rad/sec	0

CSMat: BaseDataAge 1

age	samples	0
-----	---------	---

VisionBody: Base BasePos BaseVel BaseDataAge Sample

Elbow, body at flexible arm elbow

CSMat: ElbowPos 3

x	m	0
y	m	0
theta	rad	0

CSMat: ElbowVel 3

x	m/sec	0
y	m/sec	0
theta	rad/sec	0

CSMat: ElbowDataAge 1

age	samples	0
-----	---------	---

VisionBody: Elbow ElbowPos ElbowVel ElbowDataAge Sample

Tip, body at flexible arm tip

CSMat: TipPos 3

x	m	0
y	m	0
theta	rad	0

CSMat: TipVel 3

x	m/sec	0
y	m/sec	0
theta	rad/sec	0

CSMat: TipDataAge 1

age	samples	0
-----	---------	---

VisionBody: Tip TipPos TipVel TipDataAge Sample

Because the d2a component checks the sizes, we need a different gain and

offset matrix for each size of output matrix => for each type of

object...

#

The gains are in bits/meter. Since there are 4096 bits in 20 volts,

204.8 is 1 volt per meter. Different gains may be desired for

velocities, etc. Change them here.

#

CSMat: BodyD2AGains 3

x	bits/m	20480	Note: (×100)
y	bits/m	20480	(×100)
theta	bits/m	2048	(×10)

CSMat: BodyD2AOffsets 3

x	bits	0
y	bits	0
theta	bits	0

CSMat: ElbowD2AOffsets 3

x	bits	-11469
y	bits	-6779
theta	bits	0

Note: Specific for this thesis, this is
the offset to minimize the rest position
output on the D/A

CSMat: TipD2AOffsets 3

x	bits	-4670
y	bits	-18186
theta	bits	0

CSMat: BaseD2AGains 1

theta	bits/m	2048
-------	--------	------

CSMat: BaseD2AOffsets 1

theta	bits	0
-------	------	---

#

```
# Instance the D2A drivers. Each matrix can be output individually.
#
vmic4120: Elbowd2a ElbowPos BodyD2AGains ElbowD2AOffsets 0 0X00c0b000 Sample
vmic4120: Tipd2a TipPos BodyD2AGains TipD2AOffsets 3 0X00c0b000 Sample
vmic4120: Based2a BasePos BodyD2AGains BodyD2AOffsets 6 0X00c0b000 Sample
```

setup.describe

```
#####
#
# Describe the objects
#
# Descriptions of bodies have the form:
#
# body describe
# <name>
# target locations (3 xy pairs)
# target height
# number of ports (A port is any location of interest on the body; normally 0)
# port locations (omit if 0 ports)
# tracking divisor (usually 1)
# mass & inertia (ignore, usually 0)
#
body describe
Base
0.0 0.0
-0.06 0.015
-0.06 0.0
0.044
0
1
0.0 0.0
#
body describe
Elbow
0.021 -0.021
0.007 0.013
-0.015 0.0
0.037
0
1
0.0 0.0
#
body describe
Tip
0.0 -0.03
0.014 0.0265
-0.03 0.0
0.037
0
1
```

0.0 0.0
#

setup.exe

```
#####  
#  
# Set up the execution list  
#  
dynlist select Elbow  
dynlist select Tip  
dynlist select Base  
dynlist save npgs  
dynlist activate npgs  
#  
observer select Null  
#  
matrix install byname ElbowPos  
matrix install byname ElbowVel  
matrix install byname TipPos  
matrix install byname TipVel  
matrix install byname BasePos  
matrix install byname BaseVel  
#
```

These files are setup for this experiment. They provide a good reference for other experiments as well.

There are also reference manuals for the system contained at the laboratory.
The points of contact for the *VisionServer* system are:

Dr. Stan Schneider and Vince Chen at *Real-Time Innovations, Inc.*
Tel: (408) 720-8312
Fax: (408) 720-8419

APPENDIX B

SYSTEM MATRICES

A (Plant matrix) 24×24

A Columns 1 through 6:

0	0	0	0	0	0
0	0	0	0	0	0
0	0	0	0	0	0
0	0	0	0	0	0
0	0	0	0	0	0
0	0	0	0	0	0
0	0	0	0	0	0
0	0	0	0	0	0
0	0	0	0	0	0
0	0	0	0	0	0
0	0	0	0	0	0
0	0	0	0	0	0
0	0	0	0	0	0
0	0	0	0	0	0
-2.6238e+008	-5.3179e+006	2.7380e+008	-3.5486e+006	5.3055e+003	-1.7665e+004
-2.7532e+010	-7.0657e+008	3.0591e+010	-3.6131e+008	5.0245e+005	-1.6725e+006
1.7690e+008	3.0392e+006	-1.8142e+008	2.6457e+006	-2.0354e+004	6.5544e+004
-2.3050e+009	-3.8924e+007	2.3622e+009	-3.5089e+007	4.7656e+005	-1.8992e+006
-2.6089e+005	-4.2462e+003	2.6687e+005	-4.1274e+003	1.8386e+002	-1.8304e+003
-7.1923e+008	-1.1848e+007	7.3624e+008	-1.1231e+007	2.9950e+005	-1.6911e+006
5.4046e+004	8.9028e+002	-5.5325e+004	8.4392e+002	-2.2506e+001	-1.5015e+005
-5.0110e+008	-8.2544e+006	5.1295e+008	-7.8246e+006	2.0867e+005	-6.5481e+007
4.9317e+005	8.1238e+003	-5.0484e+005	7.7008e+003	-2.0537e+002	8.6270e+004
-6.5013e+006	-1.0709e+005	6.6551e+006	-1.0152e+005	2.7073e+003	-1.1378e+006
-1.4933e+003	-2.4599e+001	1.5286e+003	-2.3318e+001	6.2184e-001	-2.6160e+002
-1.9714e+006	-3.2475e+004	2.0181e+006	-3.0783e+004	8.2094e+002	-3.4524e+005

A Columns 7 through 12:

0	0	0	0	0	0
0	0	0	0	0	0
0	0	0	0	0	0
0	0	0	0	0	0
0	0	0	0	0	0
0	0	0	0	0	0
0	0	0	0	0	0
0	0	0	0	0	0
0	0	0	0	0	0
0	0	0	0	0	0
0	0	0	0	0	0
0	0	0	0	0	0
0	0	0	0	0	0
-6.1947e+005	-3.5516e+004	1.0644e+006	-1.1069e+004	1.5520e+001	-3.2960e+000
-5.8648e+007	-3.3625e+006	1.0077e+008	-1.0479e+006	1.4694e+003	-3.1204e+002
2.2958e+006	1.3162e+005	-3.9448e+006	4.1021e+004	-5.7519e+001	1.2215e+001
-6.6970e+007	-3.8395e+006	1.1507e+008	-1.1966e+006	1.6779e+003	-3.5632e+002
-6.6409e+004	-3.8074e+003	1.1411e+005	-1.1866e+003	1.6638e+000	-3.5333e-001
-6.0350e+007	-3.4600e+006	1.0370e+008	-1.0783e+006	1.5120e+003	-3.2110e+002
-2.6370e+008	-5.3393e+006	2.7515e+008	-3.5694e+006	6.0851e+003	-1.2929e+003
-2.7699e+010	-7.1104e+008	3.0792e+010	-3.6404e+008	5.7731e+005	-1.2264e+005
1.8176e+008	3.1203e+006	-1.8642e+008	2.7222e+006	-2.3198e+004	4.8401e+003
-2.4629e+009	-4.1529e+007	2.5240e+009	-3.7573e+007	5.6752e+005	-1.3300e+005
-6.0001e+	-9.7415e+003	6.1374e+005	-9.5233e+003	4.6746e+002	-1.5088e+002
-7.7718e+008	-1.2772e+007	7.9556e+008	-1.2173e+007	3.6121e+005	-9.7577e+004

A Columns 13 through 18:

1	0	0	0	0	0
0	1	0	0	0	0
0	0	1	0	0	0
0	0	0	1	0	0
0	0	0	0	1	0
0	0	0	0	0	1
0	0	0	0	0	0
0	0	0	0	0	0
0	0	0	0	0	0
0	0	0	0	0	0
0	0	0	0	0	0
0	0	0	0	0	0
-2.0481e+003	-2.7550e+001	1.7773e+003	-1.9274e+001	2.0718e-001	2.5214e-001
-1.2644e+005	-4.7556e+003	1.5563e+005	-1.3641e+003	1.3108e+001	-2.7921e+000
1.3917e+003	1.2529e+001	-1.4958e+003	3.1263e+001	9.4949e-001	-2.1226e-001
-1.7901e+004	-1.5648e+002	1.9060e+004	-4.8544e+002	5.7886e+001	-8.8929e+001
-1.9271e+000	-1.6223e-002	2.1141e+000	-1.3180e-002	-1.5200e-002	-2.1869e-001
-5.4637e+003	-4.5895e+001	5.7527e+003	-1.5984e+002	6.5974e+001	-1.5636e+002
2.9835e+000	6.7566e-002	1.8467e+000	-1.0543e+000	2.1907e+000	8.8401e+000
-1.6551e+003	-2.5068e+001	1.5926e+003	-2.3864e+001	1.5078e+001	-6.1425e+002
-6.5206e-002	1.4592e-002	2.7265e+000	-9.8728e-001	2.5252e+000	4.2233e+000
1.1009e+001	-2.1449e-001	-6.9045e+001	4.3647e+000	8.6069e+000	-4.0245e+001
5.6003e-003	-5.6361e-005	-1.3079e-002	2.2613e-004	-7.8583e-002	-7.6421e-003

7.3721e+000	-7.3807e-002	-2.0839e+001	-3.7006e-001	-2.4475e+000	-8.5091e+000
-------------	--------------	--------------	--------------	--------------	--------------

A Columns 19 through 24:

0	0	0	0	0	0
0	0	0	0	0	0
0	0	0	0	0	0
0	0	0	0	0	0
0	0	0	0	0	0
0	0	0	0	0	0
1	0	0	0	0	0
0	1	0	0	0	0
0	0	1	0	0	0
0	0	0	1	0	0
0	0	0	0	1	0
0	0	0	0	0	1
-1.1086e+001	1.0002e-001	2.7043e+000	8.1490e-002	1.9356e-002	-1.1224e-002
-3.4851e+002	1.6711e+000	2.1629e+002	4.0357e-001	2.5826e-001	-2.5936e-001
-3.0106e+000	7.1221e-001	-7.9965e+000	2.5647e-001	1.9990e-002	-1.8806e-002
7.6339e+002	-2.9170e+001	5.3671e+002	-2.3678e+000	-2.9142e-001	-2.2942e-001
1.4315e+000	-3.6204e-002	1.0940e+000	2.1656e-002	3.9756e-002	-1.1246e-002
1.0878e+003	-3.0831e+001	7.4429e+002	6.4553e+000	1.7155e+001	-3.2682e+000
-2.0338e+003	-2.7639e+001	1.7853e+003	-1.8738e+001	1.3150e+000	-2.7654e-001
-1.2653e+005	-4.7656e+003	1.5582e+005	-1.3637e+003	2.9535e+001	-6.6973e+000
1.4266e+003	1.2753e+001	-1.5089e+003	3.1997e+001	2.6114e+000	-5.7461e-001
-1.9060e+004	-1.6548e+002	2.0214e+004	-5.1969e+002	8.1755e+001	-1.8505e+001
-4.5431e+000	-3.6568e-002	4.9598e+000	-1.2535e-001	1.9969e-001	-1.1468e-001
-5.9097e+003	-4.8940e+001	6.2656e+003	-1.9339e+002	1.2829e+002	-4.4148e+001

B (Control Matrix) 24x2

0	0
0	0
0	0
0	0
0	0
0	0
0	0
0	0
0	0
0	0
0	0
5.0424e+000	-1.8668e-002
8.6320e+002	-1.7673e+000
-1.5264e+000	6.9184e-002
1.9386e+001	-2.0181e+000
2.0756e-003	-2.0012e-003
5.8274e+000	-1.8186e+000
-4.3790e-004	5.0531e+000
4.0600e+000	8.6294e+002
-3.9958e-003	-1.5637e+000

5.2675e-002	2.0630e+001
1.2099e-005	4.7471e-003
1.5973e-002	6.2633e+000

C (Observation Matrix) 6×24

C Columns 1 through 6:

0	1.0938e+004	0	-1.0938e+004	0	0
0	0	0	0	0	0
0	0	0	0	1	0
0	0	0	0	0	-1
0	0	0	0	0	0
0	0	0	0	0	0

C Columns 7 through 12:

0	0	0	0	0	0
0	1.0938e+004	0	-1.0938e+004	0	0
0	0	0	0	0	0
0	0	0	0	0	0
0	0	0	0	1	0
0	0	0	0	0	-1

C Columns 13 through 24:

0	0	0	0	0	0	0	0	0	0	0	0	0	0	0	0	0	0	0	0	0	0	0
0	0	0	0	0	0	0	0	0	0	0	0	0	0	0	0	0	0	0	0	0	0	0
0	0	0	0	0	0	0	0	0	0	0	0	0	0	0	0	0	0	0	0	0	0	0
0	0	0	0	0	0	0	0	0	0	0	0	0	0	0	0	0	0	0	0	0	0	0
0	0	0	0	0	0	0	0	0	0	0	0	0	0	0	0	0	0	0	0	0	0	0
0	0	0	0	0	0	0	0	0	0	0	0	0	0	0	0	0	0	0	0	0	0	0

D (Feedthrough Matrix) 2×6

0	0
0	0
0	0
0	0
0	0
0	0

FINITE ELEMENT MODEL MATLAB CODE

```

%%Finite EleMent Model PrograM for the FSS
%%
%%This prograM characterizes the FSS flexible appendage.
%%LCDR Bill Harrington, USN October 1995
%%
%%The flexible appendage is to be Modeled as a 6 eleMent FEM with
%%piezoceraMic actuators located on eleMents 1 and 4, and piezoceraMic
%%sensors located on eleMents 2 and 5. The elbow and tip will be treated as
%%rigid body Masses.
%%
%%
%%This Model assuMes 0.5% structural daMping, and will solve for the first
%%12 natural Modes. The degree of accuracy is suitable only for the
%%first 3 Modes (half the nuMber of eleMents, normally).
%%

clear
clc
format short e
global A B C D

%%structural properties

nuMeleMents=6;
h=[0.07 0.03 0.5688 0.07 0.03 0.549];           %%Meters
thicKness=0.0015875;
height=0.0254;
rho=2800;                                         %%Kg/M^3
elMass=rho*height*thicKness;                     %%Mass/length
clinertia=1/12*thicKness^3*height;               %%Meter^4
E=72e9;                                           %%Modulus of elasticity

%%CoMpute eleMental stiffness and Mass Matrices

KeleMent=0*ones(4,4*nuMeleMents);
MeleMent=0*ones(4,4*nuMeleMents);

for i=1:nuMeleMents,...
    KcLeMent(:,4*i-3:4*i)=E*clinertia/h(i)^3*[12 6*h(i) -12 6*h(i);...
        6*h(i) 4*h(i)^2 -6*h(i) 2*h(i)^2;-12 -6*h(i) 12 -6*h(i);...
        6*h(i) 2*h(i)^2 -6*h(i) 4*h(i)^2];
end

for i=1:nuMeleMents,...
    MeleMent(:,4*i-3:4*i)=elMass*h(i)/420*[156 22*h(i) 54 -13*h(i);...
        22*h(i) 4*h(i)^2 13*h(i) -3*h(i)^2;54 13*h(i) 156 -22*h(i);...

```

```

        -13*h(i) -3*h(i)^2 -22*h(i) 4*h(i)^2];
end
%%Construct global Mass and stiffness Matrices

M=0*ones(2*(nuMeleMents+1));
K=0*ones(2*(nuMeleMents+1));

for i=1:nuMeleMents,...
    M(2*i-1:2*i+2,2*i-1:2*i+2)=M(2*i-1:2*i+2,2*i-1:2*i+2) + MeleMent(:,4*i-3:4*i);
end

for i=1:nuMeleMents,...
    K(2*i-1:2*i+2,2*i-1:2*i+2)=K(2*i-1:2*i+2,2*i-1:2*i+2) + KeleMent(:,4*i-3:4*i);
end

%%Clean up
clear elinertia;

%%Fix for fixed boundry condition (row,coluMns 1&2 =0)

M=M(3:2*(nuMeleMents+1),3:2*(nuMeleMents+1));
K=K(3:2*(nuMeleMents+1),3:2*(nuMeleMents+1));

M(5,5:8)=M(5,5:8)-MeleMent(1,13:16);
M(6:8,5)=M(6:8,5)-MeleMent(2:4,13);

K(5,5:8)=K(5,5:8)-KeleMent(1,13:16);
K(6:8,5)=K(6:8,5)-KeleMent(2:4,13);

clear KeleMent MeleMent;

%%Now add elbow and tip Masses.

Melbow=0.40823;
Mtip=0.37648;
MbeaM2=(h(1)+h(2)+h(3))*elMass;

M(5,5)=M(5,5)+Melbow+MbeaM2+Mtip;
M(11,11)=M(11,11)+Mtip;

clear Mpoint Melbow Mtip ipoint MbeaM2;

%%Define the piezo actuator and sensor eleMents

delta=thicKness/2;
tp=2*1.905e-4;
wp=0.02;
Ep=6.3e10;
d31=-1.8e-10;
eT3=1.5e-8;
rhop=7700;
Kpiezo=wp*tp*Ep*(delta^2 + delta*tp + (tp^2)/3);

```

```

Ka=Kpiezo/h(1)*[12/h(1)^2 6/h(1) -12/h(1)^2 6/h(1);...
6/h(1) 4 -6/h(1) 2;-12/h(1)^2 -6/h(1) 12/h(1)^2 -6/h(1);...
6/h(1) 2 -6/h(1) 4];
Ks=Kpiezo/h(2)*[12/h(2)^2 6/h(2) -12/h(2)^2 6/h(2);...
6/h(2) 4 -6/h(2) 2;-12/h(2)^2 -6/h(2) 12/h(2)^2 -6/h(2);...
6/h(2) 2 -6/h(2) 4];

Mp=rhop*wp*tp; %Mass/length piezo

Ma=Mp*h(1)/420*[156 22*h(1) 54 -13*h(1);22*h(1) 4*h(1)^2 13*h(1) -3*h(1)^2;...
54 13*h(1) 156 -22*h(1);-13*h(1) -3*h(1)^2 -22*h(1) 4*h(1)^2];

Ms=Mp*h(2)/420*[156 22*h(2) 54 -13*h(2);22*h(2) 4*h(2)^2 13*h(2) -3*h(2)^2;...
54 13*h(2) 156 -22*h(2);-13*h(2) -3*h(2)^2 -22*h(2) 4*h(2)^2];

%%Add the piezo eleMent Mass and stiffness Matrices to the structure

M(1:2,1:2)=M(1:2,1:2)+2*Ma(3:4,3:4);
M(1:4,1:4)=M(1:4,1:4)+2*Ms;
M(6:8,6:8)=M(6:8,6:8)+2*Ma(2:4,2:4);
M(7:10,7:10)=M(7:10,7:10)+2*Ms;

K(1:2,1:2)=K(1:2,1:2)+2*Ka(3:4,3:4);
K(1:4,1:4)=K(1:4,1:4)+2*Ks;
K(6:8,6:8)=K(6:8,6:8)+2*Ka(2:4,2:4);
K(7:10,7:10)=K(7:10,7:10)+2*Ks;

clear Ks Ka Ms Ma Kpiezo;

%%Solve for natural frequencies and Mode shapes.

[oMega2,Phi,Psi]=cign(K,M);
oMega=sqrt(oMega2);
Hertz=oMega/2/pi;
ttl=str2mat(' Omega','Hertz',' ');
[ttl(1,:) ttl(3,:) ttl(2,:)]
[oMega Hertz]

%%Construct the a,b,c, and d Matrices for state-space forM.

%%Need More info on the piezos.

bb1=0; bb2=-d31*Ep*wp*(delta +tp/2); bb3=0; bb4=-bb2;
gaMMa=wp*h(2)/tp*(eT3-d31^2*Ep);
b1=[bb3 bb4 0 0 0 0 0 0 0 0];
b2=[0 0 0 0 bb1 bb2 bb3 bb4 0 0 0 0];
btMp=[b1' b2']; btMp2=-2*inv(M)*btMp; btMp3=-2*Phi'*btMp;
ctMp=[bb1 bb2 bb3 bb4 zeros(1,20)]/gaMMa; %sensor 1
ctMp2=[0 0 0 0 0 bb1 bb2 bb3 bb4 0 0 zeros(1,12)]/gaMMa; %sensor 2
ctMp3=[0 0 0 0 1 0 zeros(1,18)]; %e. disp.
ctMp4=[0 0 0 0 -1 zeros(1,18)]; %e. rot.
ctMp5=[zeros(1,10) 1 0 zeros(1,12)]; %t. disp.
ctMp6=[zeros(1,10) 0 -1 zeros(1,12)]; %t. rot.

```

```

a=[0*ones(12) eye(12);-inv(M)*K 0*ones(12)];
b=[0*ones(12,2);btMp2];
c=[ctMp;ctMp2;ctMp3;ctMp4;ctMp5;ctMp6]; %observation matrix
d=0*ones(6,2);
clear bb1 bb2 bb3 bb4 gaMMa b1 b2 btMp ctMp;
clear ctMp2 ctMp3 ctMp4 ctMp5 ctMp6 ctMp7 ctMp8;
clear E Ep eT3 i;
clear btMp2 cx d31 delta e elMass ep et3 height Mp rho rhop;
clear thicKness tp wp

%%Construct transformation matrix from modal to physical coordinates.

Phi_inv=inv(Phi);
PPhi=zeros(24);
PPhi(1:12,1:12)=Phi_inv;
PPhi(13:24,13:24)=Phi_inv;

PPhi_inv=inv(PPhi);

%%Insert natural structural damping, 0.5% for first two modes then 20% for rest.

damp=-2*0.005*oMega(1:2);damp2=-2*0.1*oMega(3:12); damp3=diag([damp' damp2']);
a2=[zeros(12) eye(12);-diag(oMega2) damp3];
b2=[zeros(12,2);btMp3];
c2=[c(:,1:12) zeros(6,12)]*[Phi zeros(size(Phi));zeros(size(Phi)) Phi];
d2=d;

a2m=PPhi_inv*a2*PPhi;
A=clean(a2m,1e-6);
b2m=PPhi_inv*b2;
B=clean(b2m,1e-6);
c2m=c2*PPhi;
C=clean(c2m,1e-7);
D=d;

%%Set an initial condition (tip displaced by 3 cm)
x0=[0 0 0 0 0.02 0 0 0 0 0 -0.03 0 zeros(1,12)];

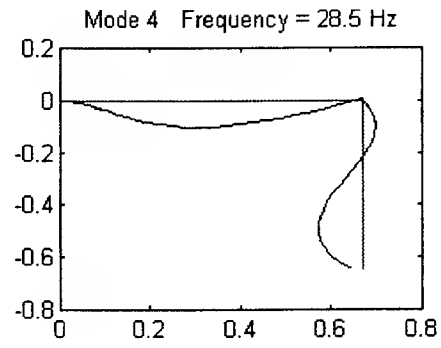
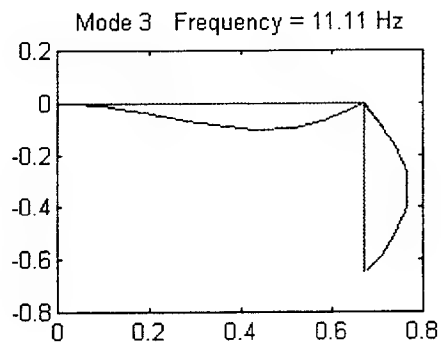
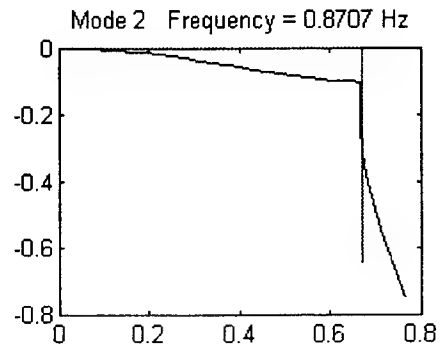
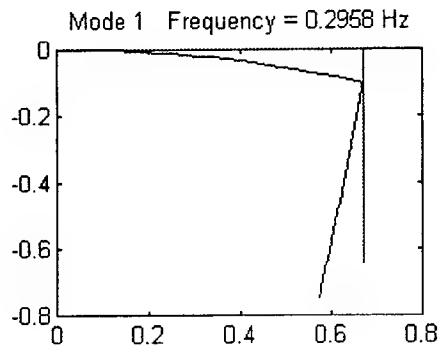
%%Time vector, t
t=0:0.01:30;

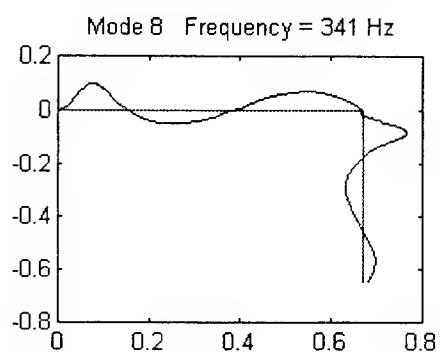
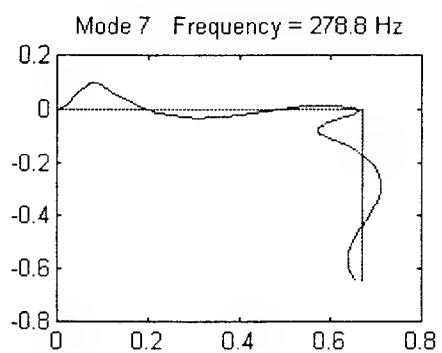
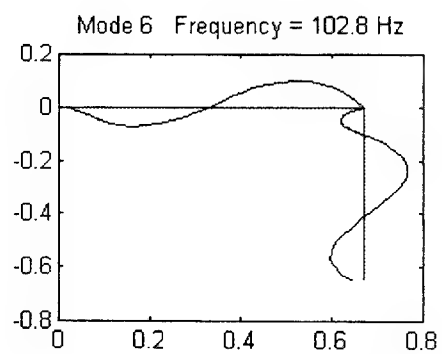
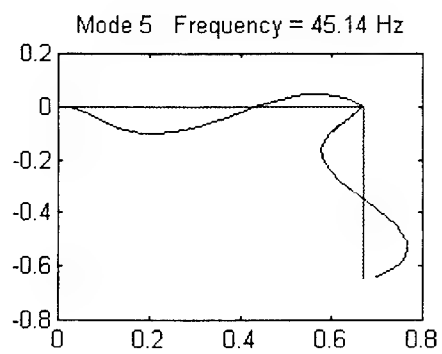
disp('Initialization of variables complete for two beam analysis. (FEM3)')

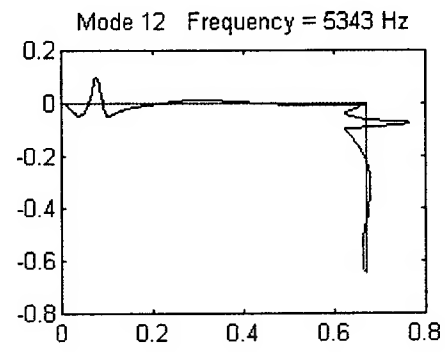
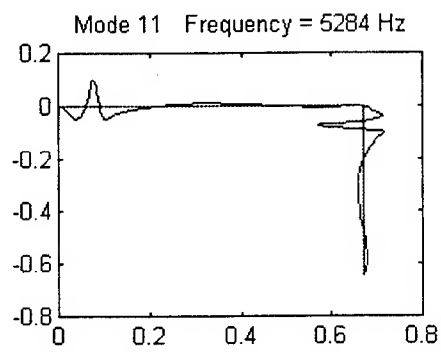
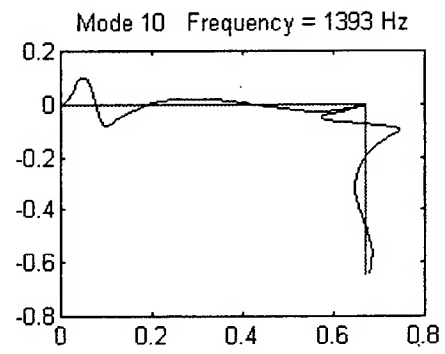
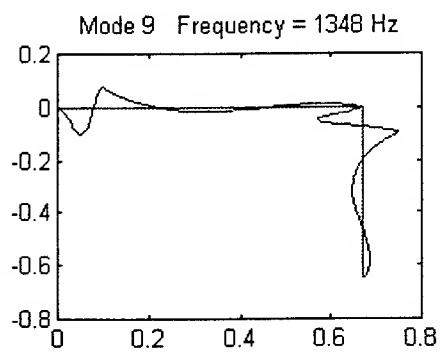
```


APPENDIX C

ANALYTICAL MODEL MODESHAPES







INITIAL DISTRIBUTION LIST

	No. Copies
1. Defense Technical Information Center 8725 John J. Kingman Rd., STE 0944 Ft. Belvoir, VA 22060-6218	2
2. Library, Code 013 Naval Postgraduate School Monterey, CA 93943-5101	2
3. Chairman, Code AA Department of Aeronautical and Astronautical Engineering Naval Postgraduate School Monterey, CA 93943-5106	1
4. Chairman, Code SP Space Systems Academic Group Naval Postgraduate School Monterey, CA 93943-5110	1
5. Professor Brij N. Agrawal, Code AA/Ag Department of Aeronautical and Astronautical Engineering Naval Postgraduate School Monterey, CA 93943-5106	2
6. Professor Roberto Cristi, Code EC/Cx Department of Electrical and Computer Engineering Naval Postgraduate School Monterey, CA 93943-5121	2
7. Professor John L. Meyer, Code AA/My Department of Aeronautical and Astronautical Engineering Naval Postgraduate School Monterey, CA 93943-5106	2
8. Commander, Naval Space Command Attn: N112 5280 4 th Street Dahlgren, VA 22448-5300	1

- | | | |
|-----|---|---|
| 9. | Assistant Commander for Space Technology
Naval Research Laboratory
Code 9110
Attn: Lieutenant Commander Barbara Bell
4555 Overlook Ave. SW
Washington, DC 20375-5000 | 1 |
| 10. | Captain S. Thomson, USN
Office of the Chief of Naval Operations
Code N63, Room 4E679, The Pentagon
Washington, DC 20350-2000 | 1 |
| 11. | Assistant Commander for Space Technology
Naval Research Laboratory
Code 9110
Attn: Lieutenant Commander William B. Harrington, Jr.
4555 Overlook Ave. SW
Washington, DC 20375-5000 | 2 |